The $z \lesssim 1$ drop of cosmic dust abundance in a semi-analytic framework

Massimiliano Parente [1,2]★ Cinthia Ragone-Figueroa [2,3] Gian Luigi Granato [2,3,4] and
Andrea Lapi [1,4,5,6]

[1] *SISSA, Via Bonomea 265, I-34136 Trieste, Italy*
[2] *INAF, Osservatorio Astronomico di Trieste, via Tiepolo 11, I-34131 Trieste, Italy*
[3] *Instituto de Astronomía Teórica y Experimental (IATE), Consejo Nacional de Investigaciones Científicas y Técnicas de la República Argentina (CONICET),*
Universidad Nacional de Córdoba, Laprida 854, X5000BGR Córdoba, Argentina
[4] *IFPU–Institute for Fundamental Physics of the Universe, Via Beirut 2, I-34014 Trieste, Italy*
[5] *INFN–National Institute for Nuclear Physics, Via Valerio 2, I-34127 Trieste, Italy*
[6] *INAF–Istituto di Radio-Astronomia, Via Gobetti 101, I-40129 Bologna, Italy*

ABSTRACT

Observations suggest that the amount of galactic dust in the Universe decreased by a factor of ∼2–3 during the last ∼8 Gyr. However, cosmological models of galaxy evolution usually struggle to explain this decrease. Here, we use the semi-analytic model (SAM) L-Galaxies2020 to show that this drop may be reproduced assuming standard prescriptions for dust production and evolution. We extend the SAM with (i) a state-of-the-art dust model that adopts the two-size approximation and (ii) a new disc instability criterion that triggers bulge and central black hole growth. The model reproduces some fundamental properties of the local galaxy population, such as the fraction of spheroid-dominated galaxies and some scaling relations involving dust. Moreover, the model predicts a galactic dust drop from $z \sim 1 \rightarrow 0$, which becomes closer to the observed one when adopting the new treatment of disc instabilities. This result is related to the newly implemented supermassive black hole growth during disc instabilities, which enhances the quenching of massive galaxies. Consequently, these objects feature a lower gas and dust content. We provide a census of the contribution of all the processes affecting the galactic dust content. Accretion is the dominant dust mass growth process. Destruction by supernovae, astration and ejection by winds have all a non-negligible role in decreasing the overall dust content in galaxies below $z \sim 1$. We also discuss predictions concerning extra-galactic dust, confirming that a sputtering efficiency lower than the canonical one is required to match the few available observations.

Key words: galaxies: evolution – galaxies: formation – galaxies: general – galaxies: ISM – dust, extinction.

1 INTRODUCTION

Dust grains are small (~ 1–10^{-3} μm) solid particles made of heavy metals polluting the interstellar medium (ISM) of galaxies (see Galliano, Galametz & Jones 2018 for a recent review). The presence of such grains heavily affects the observed spectral energy distribution (SED) of galaxies, since they absorb UV radiation and re-emit it in the IR region. These effects strongly depend not only on grain properties but also on the geometry (e.g. Granato et al. 2000). In addition, dust plays a vital role in galaxy evolution, since it actively participates in many physical processes. For example, cooling of the hot gas may be contributed by ions–grains collisions (e.g. Burke & Silk 1974; Dwek & Werner 1981; Montier & Giard 2004). The formation of H_2 molecules occurs pre-dominantly on the surface of dust grains (Wakelam et al. 2017), which are also able to shield molecular clouds from Lyman-Werner (LW) dissociating radiation. Consequently, grains play a crucial role in the whole star formation process. Moreover, radiation pressure on dust grains may stimulate the development of galactic winds (e.g. Murray, Quataert & Thompson 2005). Finally, radiation drag on dust grains may promote the accretion of low angular momentum gas to the

central supermassive black hole (SMBH) of galaxies (e.g. Granato et al. 2004).

Given its relevance, a detailed understanding of the build-up of dust in galaxies across cosmic time would be highly advantageous. In brief, dust grains are produced in stellar ejecta due to the condensation of a certain fraction of some heavy element. Asymptotic giant branch (AGB) star winds and supernova (SN) explosions are currently believed to be the leading factories of dust (e.g. Bianchi & Schneider 2007; Gail et al. 2009). However, once ejected into the ISM, several processes heavily modify the properties of grains (e.g. Dwek 1998; Zhukovska, Gail & Trieloff 2008). In dense regions, gas-phase metals may accrete onto grains, thus increasing the dust mass. On the other hand, grains may be eroded (*sputtered*) in SN shocks and by collisions with highly energetic ions in the hot plasma. Collisions between grains affect their size distribution: *coagulation* in dense environment, resulting from low-velocity ($\lesssim 0.1$–1 km s^{-1}) collisions, and *shattering* in the diffuse medium, produced by high-velocity collisions, act to shift the distribution towards large and small sizes, respectively, without affecting directly the dust mass. However, accretion and sputtering, being surface processes, are more effective on smaller grains. As a result, the mass, chemical composition, and size distribution of grains are products of the interplay between the various processes, which in turn depend on the variety of physical

conditions in the ISM (e.g. Aoyama et al. 2017; Parente et al. 2022).

All the aforementioned processes, whose relative efficiency is still uncertain and debated (e.g. Ferrara, Viti & Ceccarelli 2016; Vijayan et al. 2019; Triani et al. 2020; Dayal et al. 2022), contribute to the total budget of dust in our Universe. This quantity, commonly given in terms of $\Omega_{dust} = \rho_{dust}/\rho_{c,0}$[1], can be thought as the sum of a galactic and an extra-galactic components. In this work, we refer to them as Ω_{dust}^{ISM} and Ω_{dust}^{CGM}, respectively. In the last two decades, observations have made possible the determination of both of them, albeit with unavoidable uncertainties.

The cosmic abundance of galactic dust (Ω_{dust}^{ISM}) may be estimated by deriving the dust mass of a sample of galaxies by fitting their SED, then building a dust mass function (DMF) and integrating it. Different examples exist in the literature. Dunne et al. (2011) exploited a sample of ∼2000 sources from the Herschel-ATLAS survey, each of which with a reliable counterpart from the Sloan Digital Sky Survey (SDSS), constraining the evolution of the DMF at $z < 0.5$. They found that high-z massive galaxies have more dust than local galaxies, and that Ω_{dust}^{ISM} decreases with decreasing redshift. Driver et al. (2018) derived dust masses of ∼570 000 sources from the GAMA, G10-COSMOS, and 3D-HST catalogues over a broad redshift range (0 < $z \lesssim$ 2), finding as well a smooth decline of Ω_{dust}^{ISM} at $z \lesssim 1$. More recently, Pozzi et al. (2020) largely improved our understanding of the cosmic evolution of the DMF, by studying it up to $z \simeq 2.5$. Their results broadly confirmed what was found in past works, that is a broad peak of Ω_{dust}^{ISM} at $z \sim 1$, and then a decline towards the local Universe. Also $z \sim 0$ determinations of the DMF are available today, and are consistent with the findings highlighted above. To mention one representative work, Beeston et al. (2018) studied the DMF of a sample of $z < 0.1$ galaxies from the Herschel-ATLAS and GAMA surveys, putting precise constraints on $\Omega_{dust}^{ISM}(z \simeq 0)$.

Conversely, measurements of the amount of extra-galactic dust (Ω_{dust}^{CGM}) are more complex and, as a consequence, more scanty and uncertain. Remarkably, Ménard et al. (2010) (see also Ménard & Fukugita 2012; Peek, Ménard & Corrales 2015) derived an estimate of dust in galactic halos[2] by exploiting the reddening of distant quasars by foreground absorbers, showing that the amount of dust residing beyond galaxies is not negligible.

The result emerging from these observations, when taken as a whole (e.g. Péroux & Howk 2020, their fig. 12), is that the abundance of dust in galaxies has decreased by a factor of ∼2–3 during the last ∼ 8 Gyr. This behaviour is still not clear from a theoretical point of view. Indeed, the relatively recent inclusion of dust in some semi-analytic models (Popping, Somerville & Galametz 2017; Vijayan et al. 2019; Triani et al. 2020) and hydrodynamic cosmological simulations (McKinnon et al. 2017; Aoyama et al. 2018; Hou et al. 2019; Li, Narayanan & Davé 2019; Graziani et al. 2020; Parente et al. 2022) of galaxy evolution has made it possible to study the build-up of the DMF across cosmic epochs, investigating the role of the various processes shaping dust evolution in a cosmological context. However, most of the aforementioned works do not reproduce the observed peak of Ω_{dust}^{ISM}. Remarkable exceptions are the hydrodynamic simulations carried out by Aoyama et al. (2018) and Li et al. (2019). The first group reproduces a decline

of Ω_{dust}^{ISM} at $z < 1$, attributing it to astration, but their normalization is a factor of ∼6, too high at $z = 0$. The second group provides an excellent fit of the observed galactic Ω_{dust}^{ISM} across cosmic time. However, they do not discuss the origin of its behaviour.

Motivated by this issue, Ferrara & Peroux (2021) tried to put some constraints on the efficiency of processes acting to destroy dust, assuming that they overcome[3] the processes responsible for dust growth at $z < 1$. However, their simple computation only takes into account the efficiency of dust processes for $z < 1$, neglecting the impact of these processes on the previous evolution of Ω_{dust}.

In this work, we aim to study the Ω_{dust}^{ISM} peak at $z \simeq 1$ and its later decline in a semi-analytic framework. We focus mainly on the contribution to Ω_{dust} coming from dust inside galaxies, which is observed to drop at $z \lesssim 1$, and it is better constrained by observations. However, we also briefly discuss current observations concerning dust outside galaxies. Our goal is to assess the relative importance of the aforementioned dust-related processes in determining the decrease. A semi-analytic approach is particularly suitable for this kind of study since it allows a relatively computationally cheap exploration of the role of such processes, still considering several baryonic processes shaping galaxy evolution which may as well have a profound impact on Ω_{dust}. For this reason, we exploit the latest public release of the code L-GALAXIES2020 (Henriques et al. 2020) and extend it with a detailed treatment of dust formation and evolution in galaxies. We anticipate here that we also modify the SAM treatment of disc instabilities: besides improving the resulting morphology of the simulated galaxies, the growth of SMBH during instabilities and the consequently induced quenching turns out to be of fundamental importance for reproducing a Ω_{dust}^{ISM} consistent with observations.

The paper is organized as follows. We recap the main features of the SAM in Section 2, where we also detail the new implementation of dust evolution and disc instabilities (Sections 2.1 and 2.2). We present and discuss our results in Section 3. Here, we first check the consistency between our model predictions and some crucial quantities (Sections 3.1 and 3.2), then we show our results concerning dust in Section 3.3. The evolution of Ω_{dust} in both galactic and extra-galactic environments is discussed at length in Section 3.4. We summarize our work and present the conclusions in Section 4.

2 THE SEMI-ANALYTIC MODEL

In general, SAMs apply to DM halo merger trees approximate descriptions for the baryonic processes that are believed to be relevant in shaping galaxy populations. The merger tree can be either extracted from gravity-only simulations or calculated by Monte Carlo methods. The former possibility has become more common in the last decade. These baryonic processes now routinely include gas infall into DM halos, gas cooling, star formation, chemical and energetic feedback (the latter both from stars and AGNs), gravitational instabilities, and interactions of galaxies with the environment. The *assumed* picture is that the first outcome of gas collapse is the formation of gas discs, supported by rotation and featuring a mild star formation activity. The spheroidal component of galaxies results from galaxy mergers and instabilities, which can also produce violent starbursts if enough gas is present. The processes are described by approximate relationships between some galaxy properties (mostly mass budget in a few components and scale lengths), which are used to evolve

---

[1]Here, ρ_{dust} is the comoving dust mass density and $\rho_{c,0} = 2.775\,h^2 \times 10^{11}\,M_\odot\,Mpc^{-3}$ is the critical density of the Universe today.

[2]However, some of the absorbers selected by Ménard & Fukugita (2012) feature equivalent widths that are associated with column density typical of neutral gas, thus ISM (see section 4.2 of Péroux & Howk 2020).

[3]This is needed to obtain a decline of Ω_{dust}, since they consider both galactic and extra-galactic dust.

Table 1. List of the main physical processes modelled in the L-GALAXIES 2020 SAM. For each of them, we refer to the appropriate equations and sections of the supplementary material of Henriques et al. (2020) describing the processes and their relative implementation.

Physical Process	Reference in Henriques et al. (2020) Supplementary material	
	Equations	Sections
Gas infall into DM halos	S2	S1.3
Gas cooling into gaseous disc	S6, S7	S1.4
Spatially resolved properties of discs	S8−S11, S18	S1.5, S1.6, S1.9
H_2-based star formation	S12−S16	S1.7, S1.8
SNe feedback, gas ejection and reincorporation	S19, S23, S24	S1.10, S1.11
Chemical enrichment	S26	S1.13 and Yates et al. (2013)
SMBHs growth and feedback	S27−S29	S1.14
Environmental processes and satellites disruption	S31, S33, S34	S1.15
Mergers and starbursts	S36, S37	S1.16.1, S1.16.2
Bulges and disc instabilities	S38, S40	S1.16.3

the galaxy population over time-steps. In particular, here we adopt the public[4] semi-analytic model of galaxy evolution L-GALAXIES 2020 (Henriques et al. 2020), the latest release of the Munich galaxy formation model. This SAM is designed to run on the dark matter (DM) merger trees of the MILLENNIUM and MILLENNIUM-II simulations (Springel 2005; Boylan-Kolchin et al. 2009), We refer the reader to the L-GALAXIES papers (Henriques et al. 2015; Henriques et al. 2020), and to their supplementary material available online at https://lgalaxiespublicrelease.github.io/Hen20_doc.pdf for a complete description of the SAM. We list in Table 1 the physical processes treated by the SAM prescriptions, and the relevant sections and equations.

In the L-GALAXIES2020 model, there are a few relevant differences with respect to the previous version presented by Henriques et al. (2015). First, galactic discs (both gas and stars) are spatially resolved to some extent, i.e. they are divided into 12 concentric rings with radii $r_i = 0.01 \cdot 2^i h^{-1}$ kpc ($i = 0, \ldots, 11$) (Fu et al. 2013). Therefore, all disc properties and processes are followed for each ring separately (e.g. star formation, chemical enrichment, gas ejection). In particular, star formation is linked to the H_2 amount of each ring, which is in turn modelled according to a metallicity-dependent description (Krumholz, McKee & Tumlinson 2009; McKee & Krumholz 2009). Of particular relevance here is the inclusion of the galactic chemical enrichment (GCE) model of Yates et al. (2013), which allows tracking the amount of 11 elements, released to the gas phase by AGB stars, SNIa and SNII.

Finally, the free parameters of the SAM have been calibrated by means of an MCMC sampling technique (Henriques et al. 2009, 2015) in order to fit a number of observational constraints at $z = 0$ and $z = 2$ which we left unchanged.

We run the model on the MILLENNIUM merger trees (original box size 500/h, 2160^3 particles), adopting a *Planck* cosmology[5] (Planck Collaboration 2014) with $h = 0.673$, $\Omega_m = 0.315$, $\Omega_b = 0.0487$, $\sigma_8 = 0.829$. We adopt a Chabrier (2003) initial mass function (IMF). In selecting galaxies for our analysis, we consider both central and satellite galaxies with $\log M_*/M_\odot > 8.5$ and $\log M_{HI}/M_\odot > 8$.

2.1 Dust production and evolution

The dust formation and evolution model implemented in this work is conceptually similar to that implemented recently by our group (Gjergo et al. 2018; Granato et al. 2021; Parente et al. 2022) in hydrodynamic simulations. However, here we adapt it to the semi-analytic framework of L-GALAXIES. As in the aforementioned works, we aim to follow the mass evolution of two populations of grains with different sizes, which we will refer to as *large* and *small* grains. Indeed, we adopt the two-size approximation proposed by Hirashita (2015), who showed it to be a numerically cheap method to capture reasonably well the effects of the various processes considered in dust evolution models including grain size distribution. The method has been further validated by Aoyama, Hirashita & Nagamine (2020). Moreover, we independently follow carbonaceous and silicate dust grains. The four species pollute the cold gas, hot gas, and ejected reservoir of galaxies, where they are subjected to different processes affecting their abundance.

The aim of this section is to detail the implementation within the SAM of these processes: production by stellar sources (Section 2.1.1), shattering and coagulation (Section 2.1.2), grain growth in molecular clouds (Section 2.1.3), destruction in SNe shocks (Section 2.1.4), sputtering in the hot phase and ejected reservoir (Section 2.1.5). For the sake of clarity, we anticipate here that at each time-step of the simulation we compute the mass rate of each process and then use it to evaluate the overall mass variation of small ($_S$) and large ($_L$) grains in the cold gas, hot gas, and ejected reservoir of a galaxy:

$$\dot{M}_L^{cold} = \dot{M}_*^{cold} + \dot{M}_{coag} - \dot{M}_{shat} - \dot{M}_{astr} - \dot{M}_{SN}, \qquad (1)$$

$$\dot{M}_S^{cold} = \dot{M}_{acc} - \dot{M}_{coag} + \dot{M}_{shat} - \dot{M}_{astr} - \dot{M}_{SN}, \qquad (2)$$

$$\dot{M}_L^{hot} = \dot{M}_*^{hot} - \dot{M}_{spu}, \qquad (3)$$

$$\dot{M}_S^{hot} = -\dot{M}_{spu}, \qquad (4)$$

$$\dot{M}_{L,S}^{ej} = -\dot{M}_{spu}. \qquad (5)$$

In the above equations, $\dot{M}_*$ is the dust produced by stars, which are assumed to enrich both the cold and the hot gas with large grains, $\dot{M}_{acc}$ is the dust grown by metal accretion, acting on small grains only. The $\dot{M}_{shat}$ and $\dot{M}_{coag}$ terms describe the shattering and coagulation processes, which exchange mass between small and large grains, without modifying the total dust budget. $\dot{M}_{astr}$ is the dust removed from the cold gas phase during star formation by astration, and $\dot{M}_{SN}$ is the dust destroyed in SN shocks. $\dot{M}_{spu}$ is the term describing thermal sputtering, which we model for dust in both the hot gas and ejected reservoir.[6] In the following, we give a detailed description

---

[4]The source code is available at https://github.com/LGalaxiesPublicRelease/LGalaxies_PublicRepository/releases/tag/Henriques2020.

[5]The original MILLENNIUM cosmology has been scaled according to Angulo & White (2010) and Angulo & Hilbert (2015).

[6]The ejected reservoir is an extra-galactic component made of hot gas that cannot cool. It is enriched by SN-driven winds and such material may be reincorporated into the hot gas, making it available again for

of the processes mentioned above. Most of them are modelled by computing an associated time-scale τ_{process}, from which the mass rate is:

$$\dot{M}_{\text{S,L}}^{\text{cold,hot,ej}} = \frac{M_{\text{S,L}}^{\text{cold,hot,ej}}}{\tau_{\text{process}}}. \tag{6}$$

We note that in all the processes described by the SAM which cause gas mass transfer between components (e.g. in the ejection of cold gas by SN-driven winds, in cooling from hot to cold gas, in galaxy mergers, etc.), we generally assume that dust is preserved. These variations of dust content are not described by the above equations, where we instead highlight astration, since, in this case, dust is immediately destroyed and not just moved from one component to another.

2.1.1 Stellar production

Following Hirashita (2015), stellar populations enrich their surrounding medium with gas metals and large dust grains. In particular, winds of AGB stars and SN ejecta are expected to be the main production sources of grains. In this work, we rely on the chemical enrichment model adopted by the SAM (Yates et al. 2013), which allows tracking the chemical enrichment of eleven individual elements from SNII, SNIa, and AGB stars. We assume that a certain fraction of these elements, specified in the following, condense into dust grains. Before going into details, we anticipate a few features of our implementation.

(i) We assume that dust may be produced only by AGB stars and in SNII ejecta, thus we neglect the contribution of SNIa (see e.g. Gioannini et al. 2017; Li et al. 2019; Parente et al. 2022).

(ii) Stellar populations enrich with metals and dust both cold and hot gas, according to the assumptions of the SAM.[7] Namely, disk SNII have an enrichment efficiency of the hot gas $f_{\text{SNII, hot}} = 0.3$, while for AGB stars $f_{\text{AGB, hot}} = 0.0$. Bulge and ICL stars enrich only the hot medium.[8]

(iii) We consider two chemical compositions of dust: carbonaceous and silicate grains. The former is made only of C atoms, while we assume an olivine-like composition $MgFeSiO_4$ for silicates.

AGB stars are assumed to form carbonaceous or silicate grains, depending on the C/O number ratio in the ejecta. Indeed, since the ejecta are mixed at the microscopic level, the maximum possible amount of CO is formed before grain condensation, leaving available only the remaining C or O atoms (e.g. Dwek 1998). When C/O > 1, AGB stars produce carbon dust using the C atoms not locked into CO:

$$M_{\text{C dust}} = \max\left[\delta_{\text{AGB,C}}\left(M_{\text{C ej}} - 0.75 M_{\text{O ej}}\right), 0\right], \tag{7}$$

cooling. The ejection/reincorporation prescriptions adopted by the SAM (see supplementary material of Henriques et al. 2020) are tailored to stop star formation for relatively long periods in low-mass systems. The position of the ejected reservoir is not specified, so its physical interpretation is ambiguous (see Section 3.4.2).

[7] See also Yates et al. (2021) for a discussion on the direct hot phase metal enrichment by stars.

[8] This hot gas dust enrichment due to bulge and ICL stars has negligible impact on our results: our findings are almost unchanged when assuming that dust produced by bulge and ICL stars is destroyed when released into the hot gas. The main contribution to the dust enrichment of hot gas comes from stellar driven winds, which move dust from the cold to the hot gas.

where $M_{\text{X ej}}$ is the ejected mass of the X element and 0.75 is the ratio between O and C atomic weights. We set the condensation efficiency $\delta_{\text{AGB, C}} = 0.1$.

AGB stars produce silicates when C/O < 1. In order to preserve the chemical composition of Olivine, we first evaluate the element which constitutes a *bottleneck* for its formation. This element, often referred to as *key element* (see e.g. Zhukovska et al. 2008), is the one that minimizes the ratio between the number of atoms ejected and the number of atoms entering the compound. This value sets the number of units of $MgSiFeO_4$ that may form in the ejecta, that is:

$$N_{\text{sil}} = \delta_{\text{AGB,sil}} \min_{X \in [\text{Mg,Fe,Si,O}]} \left(\frac{M_{\text{X ej}}}{\mu_X N_{\text{ato}}^X}\right), \tag{8}$$

where μ_X is the atomic weight of the element, N_{ato}^X the number of X atoms in the compound, and $\delta_{\text{AGB, sil}} = 0.1$. Once N_{sil} is computed, the mass of each element $X \in [\text{Mg, Fe, Si, O}]$ condensing into dust is simply given by:

$$M_{\text{X dust}} = N_{\text{sil}} \mu_X N_{\text{ato}}^X. \tag{9}$$

Differently from AGB stars, in SNII ejecta the formation of carbon and silicate dust grains are not mutually exclusive, because their ejecta are not mixed at the microscopic level. Thus we evaluate the mass condensed into dust grains in SNII ejecta as

$$M_{\text{C dust}} = \delta_{\text{SNII,C}} M_{\text{C ej}} \tag{10}$$

for carbon grains and

$$M_{\text{X dust}} = N_{\text{sil}} \mu_X N_{\text{ato}}^X. \tag{11}$$

for silicates, being $X \in [\text{Mg, Fe, Si, O}]$. In above expressions, $M_{\text{X ej}}$ is the mass of the X element ejected by SNII, and N_{sil} is computed as in equation (8), adopting $\delta_{\text{SNII, C}} = \delta_{\text{SNII, sil}} = 0.1$.

2.1.2 Shattering and coagulation

When the relative velocity of large grains, originated by ISM turbolence (e.g. Yan, Lazarian & Draine 2004), is high enough ($v \sim 1$–$10\,\text{km s}^{-1}$), such particles may collide and fragment. This process, known as *shattering* (e.g. Hirashita & Yan 2009), originates small grains. In the context of the two-size approximation adopted here, shattering simply transfers mass from large to small grains. The corresponding time-scale in our model is computed for each cold gas ring as (see Granato et al. 2021):

$$\tau_{\text{sh}} = \begin{cases} \tau_{\text{sh,0}} \left(\frac{0.01}{\text{DTG}_L}\right) \frac{\text{cm}^{-3}}{n_{\text{gas}}} & n_{\text{gas}} < 1\,\text{cm}^{-3}, \\ \tau_{\text{sh,0}} \left(\frac{0.01}{\text{DTG}_L}\right) \frac{\text{cm}^{-3}}{n_{\text{gas}}} \left(\frac{n_{\text{gas}}}{\text{cm}^{-3}}\right)^{2/3} & 1\,\text{cm}^{-3} < n_{\text{gas}} < 10^3\,\text{cm}^{-3}, \end{cases} \tag{12}$$

where $\tau_{\text{sh,0}} = 5.41 \times 10^7\,\text{yr}$, DTG_L is the dust-to-gas ratio considering large grains only, and n_{gas} is the gas density. Clearly, in our SAM some assumption is needed to use a proper gas density in the above formula. In our fiducial model, we compute n_{gas} in each ring from:

$$\rho_{\text{gas}} = \frac{\Sigma_{\text{cold gas}}}{0.1 R_{\text{cold gas}}}, \tag{13}$$

where $\Sigma_{\text{cold gas}}$ is the surface density of the cold gas in a ring, and $R_{\text{cold gas}}$ the radius of the cold gas disc (i.e. we assume the height of the disc to be 0.1 its radius). We derive n_{gas} from the above formula assuming $\mu = 1.2$. The reasons for the choice of this prescription instead of, for example, a fixed n_{gas} are briefly discussed in Appendix A.

By converse, in the densest phases of the ISM, which are molecular clouds, small grains have relative velocities low enough to allow them

to aggregate into large grains. This process, dubbed *coagulation* (e.g. Hirashita & Yan 2009), transfers mass from small to large grains, without affecting the total dust budget of the cold gas. For its implementation, we follow Aoyama et al. (2017) (see also Granato et al. 2021) and derive a time-scale:

$$\tau_{\text{coa}} = \tau_{\text{co},0} \left(\frac{0.01}{\text{DTG}_{\text{S}}} \right) \left(\frac{0.1 \,\text{km s}^{-1}}{v_{\text{coa}}} \right) \frac{1}{f_{\text{H}_2}}. \tag{14}$$

In the above expression we set $\tau_{\text{coa},0} = 2.71 \times 10^5$ yr, $v_{\text{coa}} = 0.2 \,\text{km s}^{-1}$, DTG_{S} is the dust-to-gas ratio considering only small grains, and f_{H_2} is the molecular gas fraction of the ring.

2.1.3 Accretion

In the coldest and densest phases of the ISM, gas phase metals can stick on the surface of dust grains, accreting their mass (e.g. Dwek 1998). This is the *grain growth* or *accretion* process and is expected to be efficient in molecular clouds. In this work, we model the accretion time-scale for each element X following Hirashita & Kuo (2011) (see also Granato et al. 2021):

$$\tau_{\text{acc,X}} = \frac{a f_{\text{X}} s \mu_{\text{X}}}{3 n Z_{\text{X}} \bar{\mu} S} \left(\frac{2\pi}{m_{\text{X}} kT} \right)^{0.5} \frac{1}{f_{\text{H}_2}}. \tag{15}$$

In the above expression, $S = 0.3$ is the sticking efficiency, $T = 50$ K and $n = 10^3 \,\text{cm}^{-3}$ the temperature and the density assumed for molecular clouds, μ_{X} and m_{X} the atomic weight and mass of the element, $\bar{\mu}$ the mean molecular weight, f_{X} the mass fraction of the element in the grain, and Z_{X} the gas phase mass fraction of the element. The material density s is assumed to be $s = 2.2 \,\text{g cm}^{-3}$ and $s = 3.3 \,\text{g cm}^{-3}$ for carbonaceous and silicate grains. f_{H_2} is the molecular gas fraction of the ring, and a is the grain radius. Following Hirashita (2015), we assume this surface process works only for small grains, since the surface–mass ratio is larger for them. We use the representative radius $a = 0.005 \,\mu\text{m}$ for small grains in the previous equation (see Granato et al. 2021).

The accretion time-scale is evaluated at each time-step, for each element, and in each ring. For carbon grains, we adopt the time-scale obtained with equation (15). For the elements of silicate grains (O, Si, Mg, and Fe) we adopt the accretion time-scale of the element which maximizes it; this is needed to preserve the olivine-like chemical composition adopted in this work.

2.1.4 Destruction in SNe shocks

Dust grains may be efficiently eroded in shocks derived from SNae explosions, primarily by kinetic sputtering. Our model of dust destruction in SNae shocks is inspired by Asano et al. (2013) and acts on both small and large grains. For each cold gas ring, we evaluate the time-scale of the process as:

$$\tau_{\text{des,SN}} = \frac{M_{\text{cold}}}{\epsilon_{\text{SN}} M_{\text{swept}} R_{\text{SN}}}, \tag{16}$$

where M_{cold} is the mass of the gas ring, M_{swept} is the gas mass swept by an SN event, R_{SN} is the SN rate and ϵ_{SN} is a parameter quantifying the dust destruction efficiency. Here, we follow Asano et al. (2013) (see also Yamasawa et al. 2011) in evaluating the swept mass:

$$M_{\text{swept}} = 1535 \left(\frac{Z}{Z_{\odot}} + 0.039 \right)^{-0.289} M_{\odot}, \tag{17}$$

Z being the gas metallicity of the ring. The SN rate is computed self-consistently by the SAM, and here we do not differentiate among

SNII and SNIa, so that $R_{\text{SN}} = R_{\text{SNII}} + R_{\text{SNIa}}$.[9] Finally, we assume a destruction efficiency $\epsilon_{\text{SN}} = 0.1$ (McKee 1989).

2.1.5 Sputtering

In the hot gas, grains may be eroded by *thermal sputtering*, namely collisions between grains and energetic particles. We model it through a time-scale (Tsai & Mathews 1995; Popping et al. 2017; Granato et al. 2021):

$$\tau_{\text{spu}} = \tau_{\text{spu},0} \frac{a_{0.1\,\mu\text{m}}}{\rho_{10^{-27}\,\text{g cm}^{-3}}^{\text{gas,hot}}} \left[\left(\frac{T_{\text{spu},0}}{\min(T_{\text{gas,hot}}, 3 \times 10^7 \,\text{K})} \right)^{\omega} + 1 \right], \tag{18}$$

where $\tau_{\text{spu},0} = 0.17/3$ Gyr, $T_{\text{spu},0} = 2 \times 10^6$ K, $\omega = 2.5$, $a_{0.1\,\mu\text{m}}$ is the grain radius in 0.1 μm units, $\rho_{10^{-27}\,\text{g cm}^{-3}}^{\text{gas,hot}}$ the hot gas density in 10^{-27} g cm^{-3} units, and $T_{\text{gas, hot}}$ the hot gas temperature, which we assume to be the virial temperature. The representative grain radii assumed for large and small grains are, respectively, $a_{\text{L}} = 0.05 \,\mu\text{m}$ and $a_{\text{S}} = 0.005 \,\mu\text{m}$.

The above empirical fitting formula captures, besides the increase of ion–grain collisions with plasma temperature and density, the T-dependence of sputtering yield resulting from theoretical computation (e.g. Tielens et al. 1994; Nozawa, Kozasa & Habe 2006).[10] At low T, the erosion rate rapidly increases with T, then it flattens above $\sim T_{\text{spu}, 0}$. Moreover, since sputtering is a surface process, its time-scale is proportional to grain radius.

In equation (18), we simply adopt for the hot gas density the average value obtained assuming that it fills the DM halo up to the virial radius and for the temperature the virial temperature $T_{\text{vir}} = \frac{\mu m_{\text{p}}}{2k} V_{\text{vir}}^2$:

$$\rho^{\text{gas,hot}} = \frac{M_{\text{gas,hot}}}{4\pi R_{\text{vir}}^3/3} \quad \text{and} \quad T_{\text{gas,hot}} = 35.9 \cdot \left(\frac{V_{\text{vir}}}{\text{km/s}} \right)^2 \,\text{[K]}, \tag{19}$$

where R_{vir} and V_{vir} are the virial radius and virial velocity of the halo for central galaxies, or these quantities at infall for satellites. The same prescription is adopted for dust in the ejected reservoir. In our fiducial model, we adopt a $\tau_{\text{spu}, 0}$ larger by a factor 10, i.e. we reduce the sputtering efficiency to provide a better match of the cosmic abundance of CGM dust (see discussion in Section 3.4.2). This choice only influences dust in the hot gas and ejected reservoir. In other words, the impact of sputtering on the cold phase dust is negligible.

2.2 Disc instabilities

We update the criterion for disc instabilities originally adopted in L-GALAXIES 2020, which is based on Efstathiou, Lake & Negroponte (1982). This prescription aims at determining when a disc is unstable to bar formation due to its self-gravity; this instability then redistributes the disc material, eventually funnelling material towards a bulge-like structure (e.g. Debattista et al. 2006). As a result of its attractive simplicity, this criterion has been widely adopted, often with minor modifications, by the SAM community (e.g. De Lucia et al. 2011; Lacey et al. 2016; Lagos et al. 2018), though not without criticism (Athanassoula 2008; Devergne et al. 2020; Romeo, Agertz & Renaud 2022). This secular process is fundamental to produce enough intermediate mass spheroids (e.g. Huško, Lacey & Baugh 2022), and it may also play a relevant role in BH growth at high redshift (Bournaud et al. 2011).

---

[9]We only consider SNe from disc stars.
[10]See also appendix A of McKinnon et al. (2017).

Our implementation is inspired to[11] Irodotou et al. (2019) and we extend the instability criterion in order to take into account the contribution of the gaseous disc to the stability of the whole disc (gas + stars; only stars are considered in Henriques et al. 2020). To do this, we evaluate the stability of the galactic disc by means of the parameter $\epsilon_{\rm tot}$:

$$M_{\rm disc,tot}\epsilon_{\rm tot} = M_{\rm disc,stars}\epsilon_{\rm stars} + M_{\rm disc,gas}\epsilon_{\rm gas}, \tag{20}$$

where

$$\epsilon_i = c_i \left(\frac{GM_{\rm disc,i}}{V_c^2 R_{\rm disc,i}} \right)^{0.5}, \tag{21}$$

with $i = \{{\rm stars, gas}\}$. In the above equation, V_c is the circular velocity of the host halo, M_i is the mass of the i component of the disc, R_i the scale length, and $c_{\rm stars}$, $c_{\rm gas}$ are parameters of the order of 1 (Efstathiou et al. 1982; Christodoulou, Shlosman & Tohline 1995). In our fiducial model, we set $c_{\rm stars} = c_{\rm gas} = 1$.

If $\epsilon_{\rm tot} > 1$, we consider the disc to be unstable. We then allow the gas to form stars and to accrete the central SMBH, and move stars from disc to bulge, until stability is restored. This is done by iterating over rings, from the innermost to the outermost one, and for each of them:

(i) if gas $M_{\rm gas}^{\rm ring}$ is present in the ring, we allow some of it to form disc stars and to accrete the central SMBH. In a single time-step dt, we assume that the mass available for the former processes is $M_{\rm gas,unst}^{\rm ring} = (dt/\tau) \cdot M_{\rm gas}^{\rm ring}$, where τ is proportional to the free fall time-scale of each ring, i.e.

$$\tau = \sqrt{\frac{1}{G\rho}}, \tag{22}$$

where ρ is evaluated as in equation (13).

A fraction $f_{\rm BH,\,unst}$ of the mass $M_{\rm gas,\,unst}$ accretes onto the central SMBH. This fraction is evaluated following almost the same prescription adopted by the SAM when dealing with BH growth in galaxy mergers,[12] namely:

$$f_{\rm BH,unst} = \frac{f_{\rm BH}}{1 + \left(\frac{V_{\rm BH,\,DI}}{V_{\rm vir}} \right)^2}, \tag{23}$$

where $f_{\rm BH}$ controls the accretion efficiency and the $(V_{\rm BH,\,DI}/V_{\rm vir})^2$ term introduces a dependence on the binding energy of the system since we expect that less gas concentrates in the centre of low mass systems.

This prescription was introduced initially by Kauffmann & Haehnelt (2000) to model the gas accretion of SMBH during major mergers. Such *phenomenological* recipe has been then widely adopted by the SAM community (e.g. Croton et al. 2016; Lagos et al. 2018; Izquierdo-Villalba et al. 2020) in both galaxy mergers and disc instabilities when gas is funnelled towards the centre of the galaxy and gives origin to starburst episodes. We thus adopt the same approach. In particular, in our fiducial model, during disc instabilities

we assume $f_{\rm BH} = 0.066$ as in mergers, while we adopt a $V_{\rm BH,\,DI}$, that is the virial velocity at which accretion saturates, larger by a factor of 6 than the one adopted during mergers (700 km s^{-1}). This increase is required to avoid excessive growth of SMBHs and ensuing quenching of intermediate mass galaxies. The role of the $V_{\rm BH,\,DI}$ parameter is discussed in Appendix B. Moreover, there we discuss tests simply adopting a constant $f_{\rm BH,\,unst}$. We found that $f_{\rm BH,\,unst} = 10^{-4}$ approximately reproduces the most important results of our work. Indeed, some other SAMs (e.g. Lacey et al. 2016) assume that a fixed fraction of the unstable gas accretes on the SMBH.

Once the fraction of the unstable mass accreting the BH has been determined, the residual fraction $1 - f_{\rm BH,\,unst}$ form stars.

(ii) If a stellar mass $M_{\rm stars}^{\rm ring}$ is in the disc ring, we move it to the bulge. In a single time-step dt, we perform a sub-iteration of $N_{\rm steps}$, removing at each sub-step a mass $M_{\rm stars}^{\rm ring}/N_{\rm steps}$ and re-evaluating the stability of the disc each time. This procedure avoids removing the whole stellar mass from a single ring when just a fraction of it would be sufficient to restore stability. We adopt $N_{\rm steps} = 20$, and we verified any value $N_{\rm steps} \gtrsim 10$ yields similar results.

We perform the steps above for each ring until the stability of the whole disc is restored. We update bulge sizes and bulge masses simultaneously. Since bulges are not the main topic of this paper, we refer the interested reader to Appendix C, where the computation of bulge sizes is detailed and few results are shown.

3 RESULTS

In the following sections, we present and discuss the main results of our simulations concerning the general properties of the galaxy population (Sections 3.1 and 3.2), their dust content (Section 3.3) and the cosmic dust density (Section 3.4). We will mainly focus on two runs, dubbed *FID* (our fiducial model) and *oldInsta*. Both embed our dust modelling introduced in Section 2.1. However, only the former relies on the prescriptions for disc instability detailed in Section 2.2 (in *oldInsta* the same prescriptions of Henriques et al. 2020 are adopted).

3.1 General properties

As a first benchmark for our model, in this section we show its results for some fundamental quantities: the Stellar, HI and H$_2$ Mass Function at $z = 0.0$ (respectively SMF, HIMF, and H$_2$MF) and the cosmic star formation rate density (SFRD). In our fiducial model, the first two quantities (Figs 1a and b) slightly differ from what is obtained with the original instability criterion of Henriques et al. (2020) (*oldInsta*). While the fiducial SMF is still in line with data, the HIMF underpredicts the observations at the high mass.[13] On the contrary, both the H$_2$MF (Fig. 1c) and the cosmic SFRD (Fig. 2) are in good agreement with observations when our fiducial model is adopted. In particular, the former quantity is extremely improved when compared to the recent determinations of Andreani et al. (2020) and Fletcher et al. (2020): the *oldInsta* model has too much H$_2$ in the most massive galaxies, as already discussed in Henriques et al. (2020).

We anticipate the reason for the differences outlined above: our model allows for the SMBHs growth during disc instabilities, result-

---

[11]Differently from Irodotou et al. (2019), we do not distinguish between classical bulges (formed during mergers) and pseudo-bulges (originated from disc instabilities). Another crucial difference is the division into rings of discs in the SAM we adopt. Here, we determine if a disc is unstable according to its global properties, but a ring-by-ring evaluation of the instability would also be an interesting experiment (see e.g. Stevens, Croton & Mutch 2016).

[12]Equation S27 of the supplementary material of Henriques et al. (2020), setting $M_{\rm sat}/M_{\rm cen} = 1$.

[13]This issue holds regardless of the uncertainty linked to the neutral gas fraction of the cold phase of a galaxy, here assumed to be $f_{\rm neu} = 1/1.3$ (Fu et al. 2010). Also, in the extreme case when $f_{\rm neu} = 1$ the HIMF appears to be underabundant at high masses.
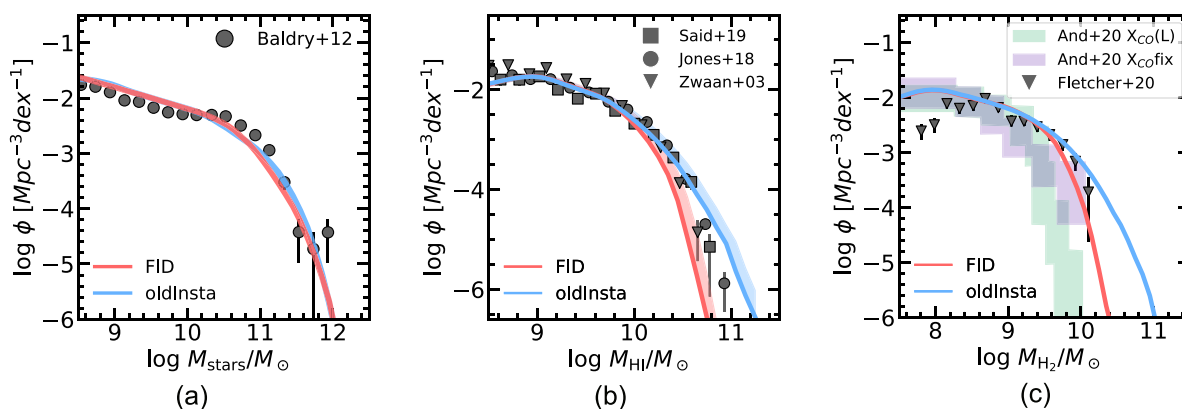
Figure 1. Mass functions at $z = 0.0$ of our fiducial model (*FID*; red) and the model without updated treatment of disc instabilities (*oldInsta*; blue). Left-hand panel: SMF compared with observations by Baldry et al. (2012). Central panel: neutral hydrogen mass function (HIMF) compared with data from Zwaan et al. (2003), Jones et al. (2018), and Said, Kraan-Korteweg & Staveley-Smith (2019). Here, we show the dispersion obtained assuming the neutral fraction to be 1/1.3 (Fu et al. 2010) or 1. Right-hand panel: molecular hydrogen mass function compared with observations by Fletcher et al. (2020) and Andreani et al. (2020). As for the latter work, we show their results obtained assuming either a constant (purple) and luminosity-dependent (green) CO conversion factor.
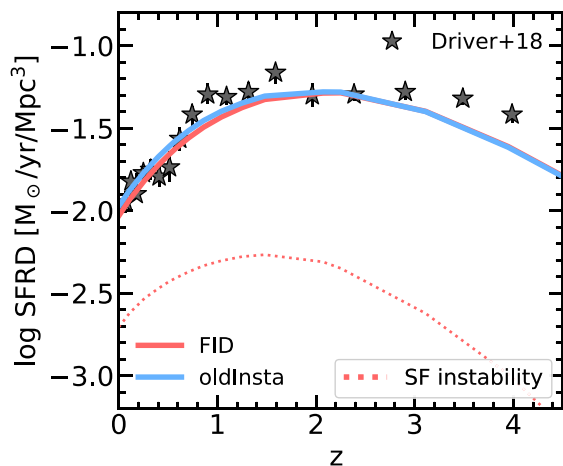
Figure 2. Cosmic evolution of the star formation rate density in our fiducial model (*FID*; red) and in the model without the new implementation of disc instabilities (*oldInsta*; blue). As for our FID model, we also show the star formation triggered by disc instability episodes (SF instability; dotted line). Data from Driver et al. (2018) are also shown for comparison.

ing in an earlier growth of SMBHs,[14] and then a faster quenching by cooling suppression due to the radio mode feedback. This results in lower gas contents (and then H_2 and star formation) when disc instabilities occur.

In conclusion, our fiducial model produces a reasonable $z = 0.0$ galaxy population and a cosmic SFRD in good keeping with the data. This holds despite some modifications we introduced on the physics implemented in the SAM, without parameter re-tuning.

3.2 Galaxy morphology and star formation

In this section, we first inspect the morphology of the model galaxies, quantified using the Bulge-to-Total stellar mass ratio (B-to-T). We

[14]Bulge and BH masses in our model remain consistent with observations (Appendix D).

show in Fig. 3 the relative fraction of disc-dominated (B-to-T < 0.3) and spheroid-dominated galaxies (B-to-T >0.3) as a function of stellar mass for our fiducial model, as well as for the model without the new implementation of disc instabilities (*oldInsta*). In the same figure, we show the results of the Galaxy And Mass Assembly survey (GAMA; Moffett et al. 2016). In their local sample of observed galaxies, these authors study the contribution of different morphological types to the total galaxy stellar mass function. They found that the transition point marking the dominance of spheroidal galaxies (E, S0-Sa, LBS[15] types) over disc-dominated galaxies (Sd-Irr, Sab-Scd types) occurs at $M_{stars} \simeq 10^{10} M_\odot$. This finding is in excellent agreement with our model predictions. The updated disc instability recipe is required to produce a reasonable number of bulge-dominated systems since the *oldInsta* model predicts a too large value of the transition mass. Disc instabilities turn out to be fundamental for bulge formation in the $10^{10} - 10^{11} M_\odot$ stellar mass range, where bulge growth by mergers is insufficient (see the detailed discussion in Irodotou et al. 2019, in the framework of L-GALAXIES 2015, or in Huško et al. 2022) and near the mass range ($3 \cdot 10^9 < M_*/M_\odot < 3 \times 10^{10}$) in which according to observations pseudobulges dominate (Fisher & Drory 2011).

Once we verified that our model reproduces the number of spheroidal galaxies observed in the local Universe, we now analyse their star formation properties. The link between galactic morphology and galaxy properties has been observed and studied for a long time (e.g. Roberts & Haynes 1994), with early type galaxies being typically redder and less star forming than late-type ones (see e.g. the recent work by Dimauro et al. 2022). Although a solid theoretical explanation for this is still missing, many SAMs (including the present one) produce passive, elliptical galaxies as a result of mergers, which trigger bulge formation and BH growth. The subsequent BH radio mode feedback prevents the cooling of the hot gas and consequently stops the star formation (e.g. Croton et al. 2006). In

[15]We include Little Blue Spheroids (LBS) in spheroidal-dominated galaxies, differently from what is done by Moffett et al. (2016). LBS are often associated with pseudo-bulges (Sérsic index $n \leq 2$). Since we do not explicitly discriminate between classical and pseudo-bulges, we include LBS in spheroid-dominated galaxies. However, we point out that their contribution is only relevant at $M_{stars} \lesssim 10^{9.5} M_\odot$.
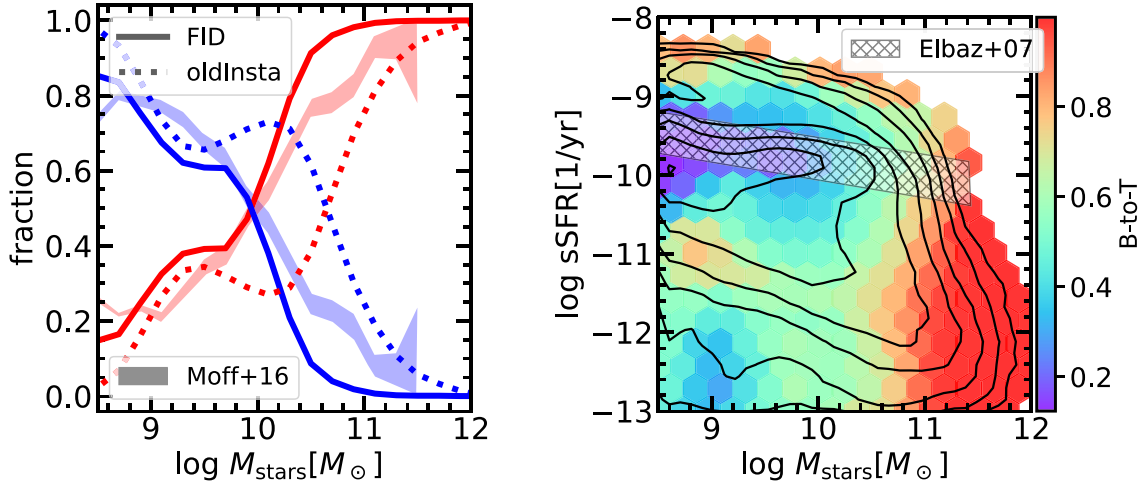
Figure 3. Left-hand panel: fraction of disc-dominated galaxies (B-to-T ≤ 0.3, blue) and spheroid-dominated galaxies (B-to-T > 0.3, red) for our fiducial model (*FID*; solid line) and the model without the updated disc instability model (*oldInsta*; dotted line). We compare with observations of Moffett et al. (2016) (coloured regions). Right-hand panel: Specific SFR as a function of stellar mass at $z = 0.0$ for our fiducial model. The bins of the 2D histogram are coloured according to the mean B-to-T, while log-spaced density contours are shown as black lines to give a qualitative idea of the distribution of galaxies in this plane. We overplot the Elbaz et al. (2007) SF main sequence as a grey hatched region.
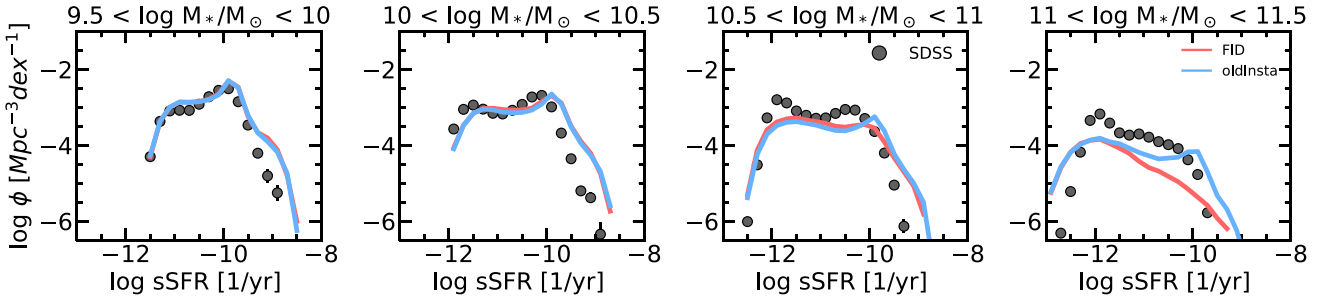
Figure 4. Specific SFR distribution for our $z = 0.0$ sample of galaxies with log SFR> $10^{-1.5}$ $M_\odot$ yr^{-1} in stellar mass bins of width $\Delta \log M_*/M_\odot = 0.5$. Our model (*FID*; red) is compared with the model without the updated implementation of disc instabilities (*oldInsta*; blue). Data from SDSS-DR7 (Katsianis et al. 2020) are shown in each panel as filled circles.

our specific case, we introduce a new BH-growth channel, namely gas accretion during disc instabilities, and then we indirectly modify the original quenching scheme.

It is thus interesting to inspect the star formation properties of our simulated galaxies. First, in Fig. 3(b), we show the $z = 0$ distribution of our galaxies in the specific SFR (sSFR= SFR/$M_{\rm stars}$) − $M_{\rm stars}$ plane, coloured according to the mean B-to-T in each bin. We also overplot the fit to the observed SF main sequence proposed by Elbaz et al. (2007). Our simulated galaxies follow this relation up to log $M_{\rm stars}/M_\odot \lesssim 10^{10.5}$. Galaxies overlapping to the observed main sequence are principally disc-like (B-to-T $\lesssim$ 0.4). With increasing stellar mass, the passive population becomes dominant. This population typically features an elliptical structure (B-to-T $\gtrsim$ 0.7). Our model thus produces a qualitative correlation between the B-to-T and the position in the sSFR - $M_{\rm stars}$ plane, in line with observations (e.g. Dimauro et al. 2022). However, a detailed analysis of the interplay between morphology and quenching goes beyond the scope of the present work. We refer to Koutsouridou & Cattaneo (2022) for an investigation of this topic in a SAM.

A deeper analysis of the impact of the new disc instability prescription on the star formation properties of our simulated galaxies

is in Fig. 4. There, we show the specific SFR distribution in different stellar mass bins for the *FID* and *oldInsta* model, compared with SDSS-DR7 data (Katsianis et al. 2020). The two models perform similarly for log $M_{\rm stars}/M_\odot$ < 10.5, while at larger stellar masses the *FID* model is characterized by generally lower sSFRs and less bimodality. Our fiducial model reproduces the shape of the observed distribution in the most massive stellar mass bin, although with a lower normalization. On the other hand, in the same mass bin the *oldInsta* model predicts too much star forming objects, likely because of their excessive molecular gas content (see Fig. 1c).

Star formation differences between these two models are due to the enhanced SMBH growth during disc instabilities[16]: BHs in unstable galaxies grow faster and prevent the cooling with their radio-feedback, leading to more rapid quenching of the galaxy. This mechanism prevents the formation of massive, gas rich, star forming (and dust rich, see Section 3.3.1) galaxies at $z = 0.0$. However, the discussion above suggests that the current BH-driven quenching

---

[16]A few results for different choices of $V_{\rm BH, DI}$ in equation (23) are shown in Appendix B.

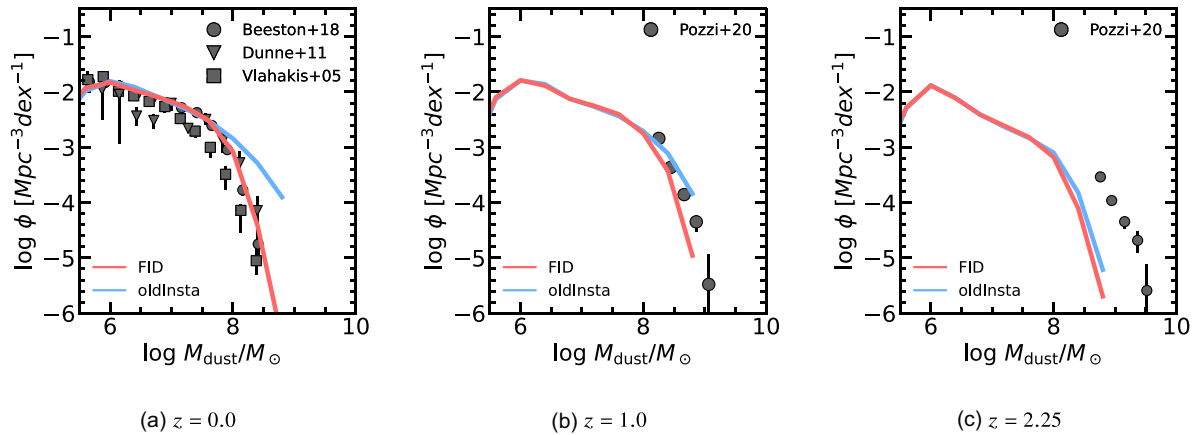(a) $z = 0.0$ (b) $z = 1.0$ (c) $z = 2.25$

Figure 5. Dust mass functions of the fiducial model (*FID*; red solid line) and the model without updated disc instability recipe (*oldInsta*; solid line) at $z = 0.0$, 1.0, and 2.25. We also report observations by Beeston et al. (2018), Dunne et al. (2011), and Vlahakis, Dunne & Eales (2005) at $z = 0.0$, and by Pozzi et al. (2020) at higher redshift.

should be further revised to match SDSS data for $\log M_*/M_\odot > 11$, where our normalization is too low.

3.3 Dust content of galaxies

To validate our dust implementation within the SAM, we now discuss some model predictions concerning dust at various redshifts. In this section, we only consider galactic dust, which corresponds to dust in the cold gas of galaxies. In this work, our primary focus concerns global galaxy properties, and thus we limit to these quantities, postponing to a future work any detailed analysis of spatially resolved dust properties.

3.3.1 Dust Mass Function

Fig. 5 shows the DMF at $z = 0.0$, $z = 1.0$, and $z = 2.25$, together with some observational determinations. The local DMF predicted by our fiducial model is in excellent agreement with the reported observations (Vlahakis et al. 2005; Dunne et al. 2011; Beeston et al. 2018), while the *oldInsta* model overpredicts the high mass end. This failure is strictly related to the HI and H_2 mass abundance of the most massive galaxies discussed in Section 3.1, as well as to the number of massive star forming objects illustrated in Fig. 4. The faster (with respect to the *oldInsta* model) quenching powered by disc instabilities in the *FID* model avoids the presence of very dust rich galaxies, which are not observed today (but instead predicted by other models, see Section 3.4). In $z > 0$ bins, we compare with results by Pozzi et al. (2020); these authors derived the DMF up to $z \simeq 2.5$ and found a characteristic dust mass increasing with redshift. Qualitatively, also our model predicts more dust rich galaxies in these $z > 0$ bins with respect to $z = 0$. However, we slightly underestimate the abundance of $\log M_{dust}/M_\odot \gtrsim 9$ high$-z$ galaxies that is observed.

Finally, since our new model of disc instabilities improved the predictions on the morphological type of simulated galaxies (Section 3.2), it may be interesting to inspect the relation between the dust content and morphology. Beeston et al. (2018) coupled their dust mass determination with the morphological classification of GAMA galaxies (Driver et al. 2012; Moffett et al. 2016) and derived the local DMF of elliptical and non-elliptical galaxies. We show their results in Fig. 6, compared with our model predictions. In keeping
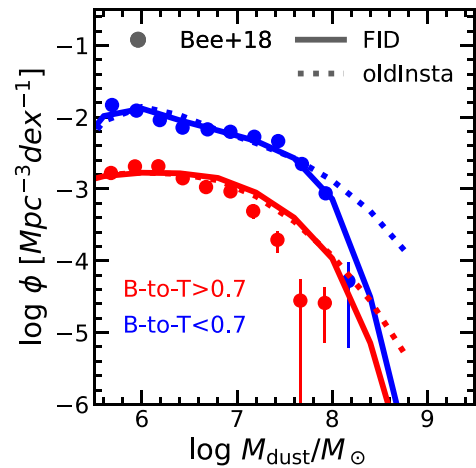

Figure 6. Dust mass function at $z = 0$ for elliptical (B-to-T > 0.7; red) and non-elliptical (B-to-T < 0.7; blue) galaxies. Results from both the *FID* and *oldInsta* models are shown (solid and dotted lines). We compare with the observations of Beeston et al. (2018).

with data, our elliptical galaxies are more dust poor than non-elliptical ones in both the *FID* and *oldInsta* model. In particular, our inclusion of disc instabilities clearly improves the match for non-elliptical galaxies at the high mass end. The elliptical galaxies DMF is instead less affected by the disc instability prescription. Both models slightly overestimate the high mass end of their observed DMF.

3.3.2 Dust, stars, and metallicity

Fig. 7 shows the relation between dust and stellar masses in our fiducial model at $z = 0.0$, $z = 1.0$, and $z = 2.25$. Observations from Beeston et al. (2018), De Vis et al. (2019) (DustPedia) and Santini et al. (2014) are used for comparison. Generally, our predictions fit well all data points. In particular, the linear relation observed at $z > 0$ redshift bins is reproduced up to $M_{dust} \sim 10^8 - 10^{8.5} M_\odot$. As highlighted in the previous section, galaxies featuring so high dust masses are not observed in the local Universe. At $z = 0$ instead, the observed $M_{stars}-M_{dust}$ exhibits a flattening towards large stellar
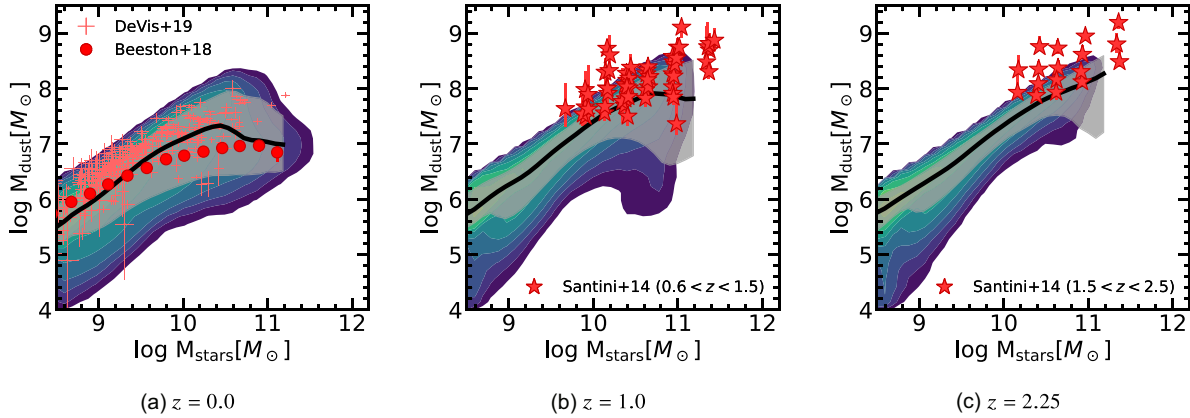
Figure 7. $M_{dust}-M_{stars}$ relation for our fiducial model at $z = 0.0$, $z = 1.0$, and $z = 2.25$. The median relation is shown as black line, while the grey shaded region refers to the 16–84th percentile dispersion. We show in background log-spaced density contours of our galaxies in this plane. Data from Beeston et al. (2018), De Vis et al. (2019), and Santini et al. (2014) are shown for comparison.
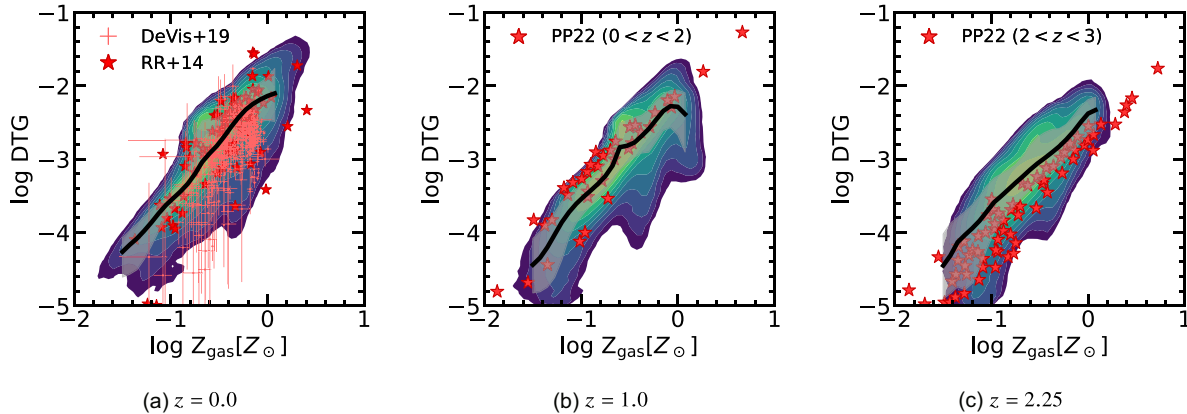

Figure 8. DTG$-Z_{gas}$ relation for our fiducial model at $z = 0.0$, $z = 1.0$, and $z = 2.25$. The median relation is shown as black line, while the grey shaded region refers to the 16–84th percentile dispersion. We show in background log-spaced density contours of our galaxies in this plane. We compare with observations by Rémy-Ruyer et al. (2014), De Vis et al. (2019), and Popping & Péroux (2022).

masses (Beeston et al. 2018, binned data), as well as our model successfully does.

The relation between ISM Dust-to-Gas ratio (DTG) and metallicity is also crucial since the accretion process relates the two quantities (e.g. Hirashita 2013). Thus, we report it in Fig. 8 at various redshifts. Observations (Rémy-Ruyer et al. 2014; De Vis et al. 2019; Popping & Péroux 2022) suggest a positive growth of DTG with gas metallicity and a nearly non-evolving relation with cosmic time (see discussion in Popping & Péroux 2022). Our fiducial model reproduces this scenario, especially at $z = 0.0$, where different observations well constrain this relation. A nice agreement with data is also obtained at $z > 0$, although we slightly overpredict DTG in the $2 < z < 3$ redshift bin. However, we also point out that no cosmological model currently reproduces this relation over a wide range of redshift; we refer interested readers to Popping & Péroux (2022) for a discussion of this issue.

Finally, we note that the lowest metallicity objects in our sample ($\log Z_{gas}/Z_\odot \sim -1.5$; $M_{stars} \sim 10^{8.5} M_\odot$) feature a very small, but *non-zero*, amount of dust, i.e. $M_{dust} \sim 10^4 M_\odot$. These objects, often referred to as extremely metal-poor galaxies, are also observed to be dust deficient (e.g. Almeida et al. 2016) and are thought to be analogous of high-z galaxies (e.g. Fisher et al. 2013; but see also Isobe et al. 2021).

3.3.3 Grain sizes

Our dust model follows two distinct dust grain sizes, i.e. small and large grains. Observationally, the determination of the relative abundance of small and large grains may be estimated with SED fitting. This estimate has been done for a sample of local galaxies in two recent works by Relaño et al. (2020) and Relaño et al. (2022), whose results are shown in Fig. 9 together with our model predictions. We caution the reader about this comparison. Indeed, while in our two size approximation the transition from small to large grains occurs at $0.03\,\mu m$, it occurs at $0.015\,\mu m$ in the model[17] adopted by Relaño et al. (2020) and Relaño et al. (2022). Moreover, they assume carbonaceous properties for small grains, while we also consider small grains to have a silicate composition.

The relation between the observed Small-to-Large grain mass ratio (S-to-L) and stellar mass (left panel) exhibits e nearly flat trend with a median value of S-to-L$\sim$0.2–0.3 and $\sim$0.7 dex dispersion. However, the more recent work by Relaño et al. (2022), who made

---

[17]The adopted cosmic dust model is that by Desert, Boulanger & Puget (1990). It takes into account polycyclic aromatic hydrocarbons (PAHs), very small grains (VSGs), and big grains (BGs). The former two are considered small grains, the latter component is the only constituent of large grains.
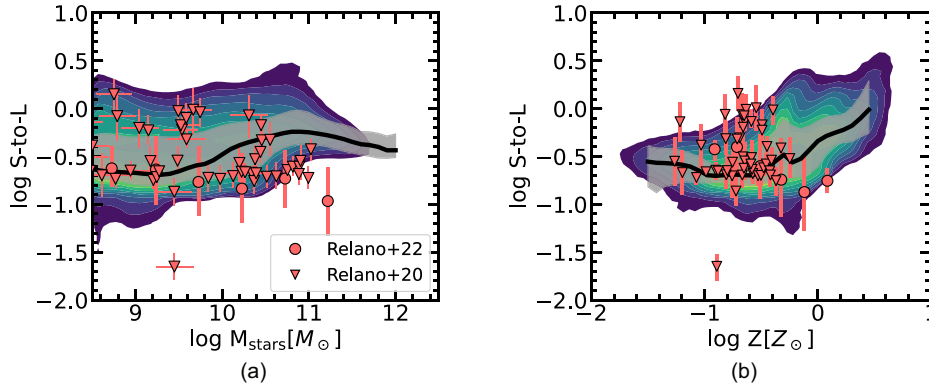
Figure 9. Small-to-large grains mass ratio as a function of stellar mass (left-hand panel) and ISM total metallicity (right-hand panel) for our fiducial model (density contours) at $z = 0.0$. The median relation is shown as black line, while the grey shaded region refers to the 16–84th percentile dispersion. We show in background log-spaced density contours of our galaxies in this plane. The SAM results are compared with observations by Relaño et al. (2020) (red triangles; both DSG and KINGFISH data) and Relaño et al. (2022) (red circles; binned data).

use of a significantly larger sample of galaxies, suggests a slowly decreasing trend of S-to-L with M_{stars}. The relationship between S-to-L and ISM metallicity (right panel) shows qualitatively similar behaviour. Although our model matches the median S-to-L, we fail in reproducing its decrease toward high M_{stars} and Z. Other cosmological simulations which adopt the two size approximation (Hou et al. 2019; Parente et al. 2022) ascribe this behaviour to the dominance of coagulation over accretion and shattering. In our model, high S-to-L galaxies at large M_{stars} or Z have typically low molecular gas fractions. Thus coagulation of small grains is not effective enough. We conclude that, although our model can reproduce the S-to-L ratio of the bulk of the observations, some improvements of the admittedly simple treatment of shattering and coagulation are required to avoid over-predicting the abundance of small grains in massive galaxies. Finally, we note that the adoption of a non-constant n_{gas} in equation (12) (see also equation (13)) has little impact on the scaling relations just discussed. Instead, it is needed to obtain reasonable results when looking at small and large grain profiles, as we discuss in Appendix A.

3.4 The cosmic evolution of dust abundance

In this section we present and discuss what we consider the most interesting result of our work, that is the cosmic evolution of the galactic, extra-galactic and total dust budget across cosmic time.

3.4.1 Galactic dust budget

The galactic dust mass density Ω_{dust}^{ISM} as a function of redshift for the two models discussed above are shown in Fig. 10, together with some observational determinations and predictions from other cosmological models. We also show the result obtained with a model in which $f_{BH, unst} = 0$ (equation 23), that is we do not allow for BH growth during disc instabilities. We compare with the observations by Vlahakis et al. (2005), Dunne et al. (2011), Beeston et al. (2018), Driver et al. (2018), Dudzevičiūtė et al. (2020), and Pozzi et al. (2020), which are obtained by integrating the observed DMF.

Both the *FID* and *oldInsta* models are in agreement with data within a factor of ~ 2. While the model without the new implementation of disc instabilities reproduces better $z \gtrsim 1$ data, our fiducial model performs better at lower redshift, in particular as far as the

observed decrease of Ω_{dust}^{ISM} is concerned. As already discussed, the different performance of these two models is strictly related to the BH accretion during disc instabilities and its effect on quenching. This is confirmed by the $f_{BH, unst} = 0$ model, which performs similarly to the *oldInsta* model and does not reproduce the desired decline of $\Omega_{dust}^{ISM}(z)$ toward $z = 0$.

Fig. 10 demonstrates that the observed $\Omega_{dust}^{ISM}(z)$ is poorly reproduced by almost all other cosmological computations (SAM or hydrodynamical simulations) published so far, which tend to overpredict the data and to produce only a very mild, if any, decrease from $z \sim 1$ to $z = 0$. The only exception is the SIMBA simulation (Li et al. 2019), which shows an Ω_{dust}^{ISM} evolution very similar to that of our fiducial model.

We now investigate *why* and *how* the galactic dust decreases from $z \sim 1$ to $z = 0$ in our fiducial model. To do this, we consider separately the rates of all the processes capable of modifying the abundance of the dust in the cold gas of our model galaxies: production by stars, accretion, dust transferred from the hot to the cold gas by cooling, destruction by SNe, ejection from cold gas, and astration. These are shown in Fig. 11 as a function of redshift, together with the sum of those contributing to a decrease(increase) of $\rho_{dust\,cold}$. Except for dust *cooled* (i.e. dust transferred from the hot to cold gas in the cooling process), all other rates roughly follow the shape of the SFRD with a certain delay. This result is expected since all of them depend directly (dust produced by stars, astration) or indirectly (destruction by SN, ejection from cold gas due to stellar feedback, accretion) on star formation. Among the processes contributing to the increase of dust, accretion is by far the dominant one ($\gtrsim 80 - 90$ per cent at least for $z \lesssim 4$, where we focus our attention). On the contrary, all destruction/ejection processes have a significant contribution to the decrease of ISM dust (destruction by SN $\simeq 45$ per cent, ejection $\simeq 35$ per cent and astration $\simeq 20$ per cent at $z = 0$).

An interesting exercise is to study what happens to Ω_{dust}^{ISM} when the destruction/ejection processes (astration, ejection from cold gas, and SN destruction) are alternatively switched off. Fig. 12 shows the result. When neglecting dust destruction by SNe (*noSNdes*), the predicted Ω_{dust}^{ISM} is very similar to our fiducial model, but for a slight increase of it, especially at high z. This behaviour is because most of the gas phase metals produced by the SNe destruction process in the *FID* model are quickly re-locked into dust grains by the accretion process. Therefore, in the *noSNdes* model, this does not happen, also
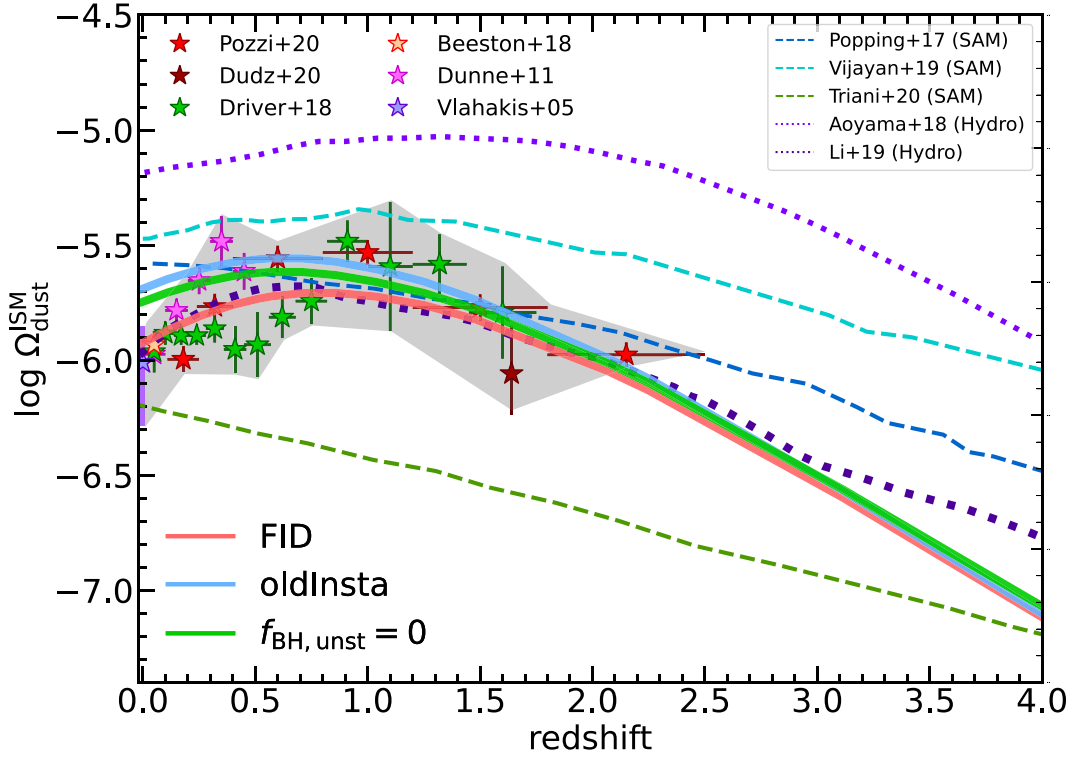
Figure 10. Cosmic ISM dust abundance across cosmic time. We show the dust abundance in cold gas for: (i) our fiducial model (*FID*; red solid line); (ii) a model without the new implementation of disc instabilities discussed in this work (*oldInsta*; blue solid line); (iii) a model without BH accretion during disc instabilities [$f_{BH, unst} = 0$ in equation (23); green solid line]. Results derived from the integration of the DMF at various redshifts are shown as stars: Vlahakis et al. (2005) (purple), Dunne et al. (2011) (pink), Beeston et al. (2018) (orange), Driver et al. (2018) (green), Dudzevičiūtė et al. (2020) (brown), and Pozzi et al. (2020) (red). A shaded grey region shows the global behaviour of these data. Results from other groups are shown as dashed (SAMs; Popping et al. 2017 in blue, Vijayan et al. 2019 in light cyan, and Triani et al. 2020 in green) and dotted (hydrodynamic simulations; Aoyama et al. 2018 in purple and Li et al. 2019 in dark blue) lines.
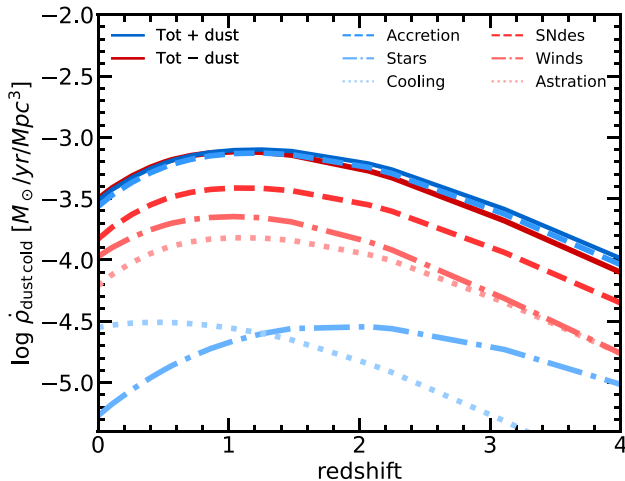
Figure 11. Cosmic evolution of the rates of the processes contributing to the overall abundance of dust in the cold gas of galaxies in our fiducial model: stellar production (blue dot-dashed), accretion (blue dashed), dust transferred from hot to cold gas by cooling (blue dotted), destruction by SN (red dashed), dust ejected from cold by stellar driven winds (red dot-dashed), and astration (red dotted). The total rate of the processes leading to an increase (decrease) of dust in the cold gas is shown as a solid blue (red) line.
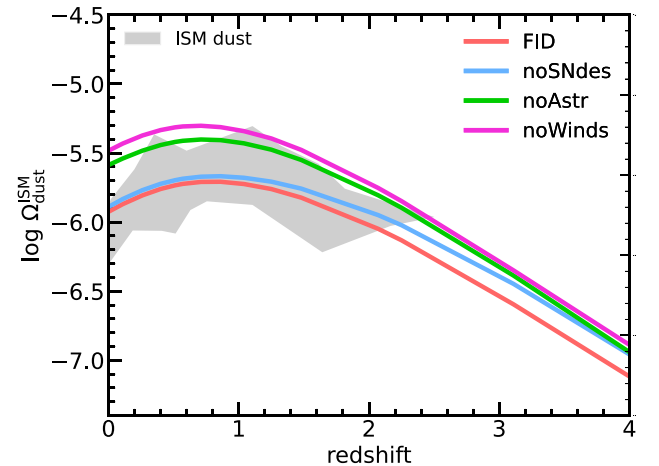

Figure 12. Cosmic evolution of galactic dust obtained by switching off one at a time the processes responsible for the dust destruction/removal in the cold gas: destruction by SNae (*noSNdes*; blue); astration (*noAstr*; green); ejection from cold gas (*noWinds*; pink). We also report for comparison our fiducial (*FID*; red) model and the compilation of observations introduced in Section 3.4.1 (grey shaded region).

accretion is reduced with respect to the *FID* model, and the final $\Omega_{\rm dust}^{\rm ISM}$ does not differ much. Thus, the decline of $\Omega_{\rm dust}^{\rm ISM}$ is present also in this model without SN destruction.

As for the importance of SN destruction, Ferrara & Peroux ([2021](#)) recently argued that the observed $\Omega_{\rm dust}$ $z \sim 1 \rightarrow 0$ drop may suggest that each SN destroys $M_{\rm des,SN} \simeq 0.45\,M_{\odot}$ of dust, much lower than $M_{\rm des,SN} \simeq 4.3\,M_{\odot}$ that, according to them, is commonly adopted. Ferrara & Peroux ([2021](#)) obtain it assuming a solar DTG (~ 0.006). Actually, in our computations we have $M_{\rm des,SN} \simeq 2.5\,M_{\odot}$ for galaxies with DTG$\simeq$DTG$_{\odot}$, but when considering the whole galaxies population we obtain a median $M_{\rm des,SN} \simeq 0.71(0.47)\,M_{\odot}$ at $z = 0(1)$, similar to the value proposed by Ferrara & Peroux ([2021](#)). We also confirm that $M_{\rm des,SN} \simeq 4.3\,M_{\odot}$ would be not acceptable. Indeed, we checked that this median value is obtained by increasing the SN destruction efficiency by a factor $\sim$6–10, and it under-predicts (by a factor $\sim$1.5–2.5) $\Omega_{\rm dust}^{\rm ISM}$ at all redshift. The accretion process is not efficient enough to re-lock all the metals destroyed by SNe into dust.

As for the other destruction/ejection processes, a similar decline of $\Omega_{\rm dust}^{\rm ISM}$ occurs when astration and ejection from cold gas are switched off, but for the normalization, which is higher than in the fiducial model, since we are shutting down channels able to remove dust grains and the metals locked in them from the cold gas. Note that this is intrinsically different from what SNe destruction does. Indeed, the latter process transfers dust metals to gas metals, still leaving them available for new accretion processes in the cold phase.

We conclude that the dust processes in our model provide a good normalization of $\Omega_{\rm dust}^{\rm ISM}$, and we have shown that none is the only one responsible for its decline. The cosmic evolution of galactic $\Omega_{\rm dust}^{\rm ISM}$ is intrinsically linked to the star formation history (and thus to the neutral gas and molecular abundance evolution in galaxies), since all processes depend on it to some degree. Our new treatment of disc instabilities and the associated SMBH growth reduces the star formation, gas, and dust content of massive local galaxies, sharpening the $\Omega_{\rm dust}^{\rm ISM}$ drop towards $z = 0$, which improves the match with low redshift data.

3.4.2 Extra-galactic dust budget

We now discuss our model predictions concerning the amount of extra-galactic dust. As anticipated in the Introduction, we have just a couple of observational determinations of the dust residing beyond the ISM of galaxies, namely the ones derived by Ménard et al. ([2010](#)) and Ménard & Fukugita ([2012](#)). In Fig. [13](#), we compare their determinations of $\Omega_{\rm dust}^{\rm CGM}$ with the dust residing in the hot halo of our model galaxies, which may be broadly identified with the CGM of galaxies. However, in the SAM framework, there exists also another extra-galactic field, namely the ejected reservoir. This component represents a reservoir of hot gas that cannot cool (differently from *hot gas*), but its physical interpretation is ambiguous. For this reason, we also report the extreme case of considering CGM dust that resides in both the hot gas and ejected reservoir. We recall that in our fiducial model, we adopt a sputtering efficiency lower by a factor of 10 than the one originally introduced by Tsai & Mathews ([1995](#)), as we anticipated in Section [2.1.5](#). This is in keeping with results by Gjergo et al. ([2018](#)) and Vogelsberger et al. ([2019](#)), from computations of dust evolution in zoom-in simulation of galaxy clusters. They found that the sputtering efficiency by Tsai & Mathews ([1995](#)) leads to a too low dust content in the ICM, with respect to recent observations based on Planck data (Planck Collaboration (XLIII) et al. [2016](#)). In this section, we provide additional evidence in favor of a lower efficiency
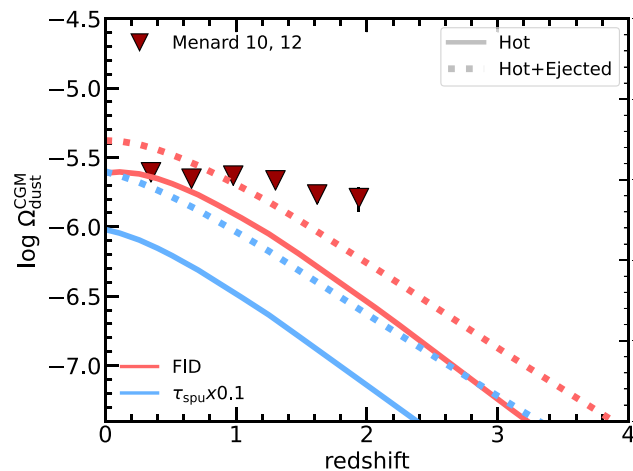

Figure 13. Cosmic evolution of dust in hot gas (solid line) and both hot gas and ejected reservoir (dotted line). The fiducial model is shown as red lines, while a model with a sputtering efficiency enhanced by a factor 10 (i.e. adopting the time-scale originally introduced by Tsai & Mathews [1995](#)) is shown as blue lines. We report observations by Ménard et al. ([2010](#)) (the lowest redshift point) and Ménard & Fukugita ([2012](#)), corresponding to CGM dust.

by showing also results obtained by a model dubbed $\tau_{\rm spu}$x0.1 which adopts the Tsai & Mathews ([1995](#)) sputtering efficiency.

When considering hot dust alone, the latter model underestimates the observations at all cosmic times by a factor 3–10, with a tension decreasing towards low z. The hot + ejected dust is instead in good agreement with observations at the lowest redshifts, but a tension of a factor $\sim$5 still exists at $z \sim 2$. Contrarily, adopting a longer sputtering time-scale as in the fiducial model helps to reproduce a CGM dust abundance more in line with observations, especially when considering both hot and ejected dust. We also note that the available observations do not allow to conclude that extra-galactic dust presents an abundance drop at $z \lesssim 1$, as observed for ISM dust. Instead, observations suggest a nearly flat trend with redshift, in tension with our steeper results; this may indicate that we are missing some physics. Indeed, although sputtering is the only dust process directly affecting the amount of dust in the hot gas (and in the ejected reservoir), this quantity also depends on several physical processes implemented in the SAM. For instance, SN driven winds are the main dust enrichment channel of the hot gas. Assuming an ejected material with a different cold gas DTG may affect our results, as well as the implementation of AGN-driven outflows, currently lacking in this model.

The good agreement obtained at low-z with a reduced sputtering efficiency is confirmed by the comparison with the work by Peek et al. ([2015](#)). These authors studied the CGM reddening of low$-z$ galaxies, deriving typical CGM dust masses of $\simeq 6 \times 10^{7}\,\rm M_{\odot}$ and a weak dependence on stellar mass for $0.1L_{*} - L_{*}$ galaxies. We thus report their results in Fig. [14](#) together with our predictions for both the fiducial and the $\tau_{\rm spu}$x0.1 model. The *FID* model allows us to capture CGM dust values found by Peek et al. ([2015](#)), and we note that considering both the hot gas and ejected reservoir as CGM dust improves the comparison with the observed, nearly flat slope of this relation.

From the comparison of the *FID* and $\tau_{\rm spu}$x0.1 models, it is clear that sputtering has a relevant role only above a certain stellar mass $M_{\rm stars} \gtrsim 10^{10}\,M_{\odot}$, where virial temperatures are high enough to make this process efficient. Moreover, in both models, ejected dust has a relevant contribution only below the aforementioned critical mass, above which SN winds are no longer efficient in
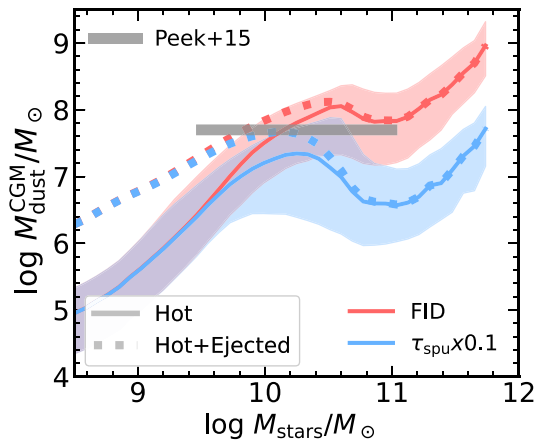
Figure 14. CGM dust as a function of stellar mass when considering dust in the hot gas (solid, with 16–84th percentiles dispersion) and both hot and ejected gas (dotted). The fiducial model is shown as red lines, while a model with a sputtering efficiency reduced by a factor of 10 is shown as blue lines. We report results by Peek et al. (2015) as a grey line.

making gas (and thus dust) able to escape from the hot halo. These qualitative findings are in keeping with what has been shown and discussed by Popping et al. (2017) and Triani et al. (2020), although within different SAM frameworks. Finally, we note that above $M_{stars} \gtrsim 10^{11} M_{\odot}$ the hot phase dust increases, since $T_{vir} \gtrsim T_{spu, 0}$, that is the temperature above which the sputtering efficiency saturates (see equation 18).

To conclude this section, we remark that the admittedly scanty information on the extra-galactic dust budget requires a lowering of the thermal sputtering efficiency, as already noted by Gjergo et al. (2018) and Vogelsberger et al. (2019) for hydro-dynamic simulations of galaxy clusters. However, we caution about the comparisons performed here since CGM dust in a SAM framework is somewhat not well defined.

3.4.3 Total dust budget

In this section, we put together the results concerning the amount of galactic and extra-galactic dust and thus discuss the cosmic evolution of the total amount of dust in our simulation. Deriving an accurate observational estimate of this quantity is a challenging task. Thus, we consider two different estimates. The first one is simply the sum of the galactic ISM (Ω_{dust}^{ISM}, that is the compilation of observations introduced in Section 3.4.1) and CGM contribution[18] (Ω_{dust}^{CGM}, Ménard et al. 2010 and Ménard & Fukugita 2012 data, Section 3.4.2). The second one is the result of Thacker et al. (2013), obtained with the observation of FIR background. This technique should capture the thermal emission of the whole population of dust grains in our Universe. Both these determinations are shown in Fig. 15, together with our model predictions. Moreover, we show results considering the CGM made either by hot gas only or hot plus ejected gas.

First, we note that our naif derivation of the total amount of dust and Thacker et al. (2013) results agree remarkably well, but at $z \lesssim 0.2$, where FIR background observations predict a weak decline of Ω_{dust}. However, we stress that our Ω_{dust} derivation is based on an

---
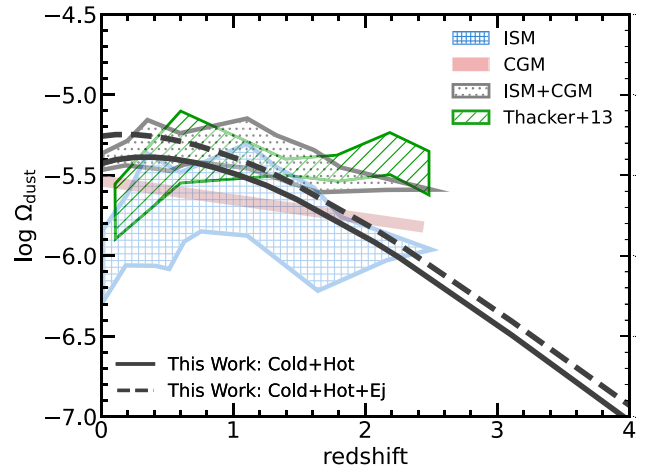
Figure 15. Cosmic evolution of the total dust budget (Cold+Hot, black solid line, and Cold + Hot + Ej, black dashed line) as predicted by our fiducial model. Shaded and hatched regions correspond to different sets of observations. ISM dust (blue hatched region) refers to the compilation of observations shown in Section 3.4.1. CGM dust (red shaded region) is obtained by performing a linear fit, extrapolated down to $z = 0$, of Ménard et al. (2010) and Ménard & Fukugita (2012) data (Section 3.4.2). Summing the above components (ISM + CGM) we obtain an estimate of the total dust content (grey hatched region). Results obtained by Thacker et al. (2013) are shown as a green hatched region.

extrapolation of CGM observations down to $z = 0$; this may constitute a source of tension. Second, our model predictions broadly reproduce observations within a factor ∼2, even better when considering the CGM made of hot + ejected gas (as already highlighted in Section 3.4.2). Our model does not reproduce any drop in the total dust budget towards $z = 0$. However, this drop is evident only for ISM data. Thacker et al. (2013) observations only constrain the whole population of (typically cold) grains responsible for the emission; a hot dust component may be thus missed. On the other hand, CGM observations, which trace the absorption of grains in typically hot environments, do not show any sign of drop up to $z \simeq 0.3$. We thus conclude that, given the available observations, our model reasonably reproduces the cosmic evolution of the total amount of dust. Future observations may better constrain its behaviour, especially for the hot, extra-galactic counterpart.

4 SUMMARY AND CONCLUSIONS

In this work, we studied the $z \lesssim 1$ drop of galactic cosmic dust from a semi-analytic model (SAM) perspective. Indeed, integration of the observed DMF in the redshift range $0 < z \lesssim 2.5$ suggests that the total amount of dust in galaxies decreased by a factor of ∼2–3 in the last ∼ 8 Gyr, albeit the reason for this is not still clear from a theoretical point of view.

We adopted the latest public version of the L-GALAXIES SAM (Henriques et al. 2020), where we have incorporated a state-of-the-art dust model and new prescriptions for disc instability. The former is based on the two-size approximation. It considers dust production by type II SNe and AGB stars, grains accretion in molecular clouds, destruction in SNe shocks, sputtering in the hot phase, and shattering of large grains and coagulation of small grains. The original model's disc instability recipe has been updated, taking into account the gaseous disc's contribution to the (in)stability of the whole disc and

---

[18]To take into account the contribution of CGM observations, we perform a linear fit extrapolated down to $z = 0$. We have no reasons to assume something more complex than this.

allowing for star formation and SMBH growth when the instability criterion is met.

This new prescription for disc instability has a non-negligible impact on galaxy evolution. First, it makes the growth of stellar bulges more efficient, leading to a better match with the observed number of local bulge-dominated galaxies. Secondly, it boosts SMBHs growth and thus indirectly enhances quenching, according to the radio-mode feedback scheme adopted in the SAM. We have tuned one of the parameters regulating SMBH growth during instabilities to keep our model predictions in agreement with local SDSS observations of the sSFR distribution. Namely, the adoption of a saturation velocity of the growth efficiency (see equation (23)) larger than a factor of 6 with respect to the one assumed in galaxy mergers, allows us to reproduce the sSFR bimodality observed at $\log M_{stars}/M_\odot \lesssim 10 - 10.5$, and to suppress the number of highly SF massive galaxies. Some other important quantities (local SMF and HIMF; cosmic SFRD; local BH-bulge mass relation) also agree with observations, as well as the H_2MF, which, without the new disc instability prescription, is slightly more abundant than the observed one.

The enhanced SMBH growth also shapes the dust properties of our simulated galaxies. While it has just a modest effect on the reproduced DMF at $z > 0$, its impact in suppressing the high mass end of the local DMF improves the match with observations. Moreover, several scaling relations involving dust ($M_{dust}–M_{stars}$; DTG–Z) turn out to be in reasonable agreement with observations at $0 < z \lesssim 2.5$. Also, the reproduced median $z = 0$ small-to-large grains mass ratio reasonably agrees with observations. However, we overproduce the mass of small grains in large M_{stars} (and Z) galaxies, suggesting that improved treatment of shattering and coagulation may be needed.

Our model allows drawing a few considerations about the behaviour of the cosmic dust density, especially the galactic component, which represents the main focus of this work. We reproduce the observed shape of the galactic cosmic dust density evolution, which is generally a challenging task for cosmological models of galaxies evolution. Specifically, when including the new treatment of disc instabilities, we obtain a more important decrease of the amount of dust in galaxies from $z \sim 1$ to $z = 0$. We found that accretion in molecular clouds is dominant among the processes contributing to the increase of galactic dust. As for processes responsible for the destruction or ejection of galactic dust, astration, destruction in SNe shocks and ejection in winds, all have a non-negligible role. In the fiducial model, their contributions to the total destruction rate of dust in cold gas are, respectively, ~ 45 per cent, ~ 35 per cent, and ~ 20 per cent at $z = 0$. Interestingly, Ω_{dust}^{ISM} only slightly increases when destruction by SNe shocks is switched off. This happens because the metals returned to the gas phase by this process are quickly re-locked into grains by accretion. Contrarily, switching off astration or dust ejection from cold gas causes an increase by a factor $\sim 2–3$ of Ω_{dust}^{ISM}.

The amount of extra-galactic dust in our model continuously grows with time. It broadly reproduces observations but with a steeper redshift evolution, especially when considering both hot gas and the ejected reservoir as CGM. This achievement has been made possible by adopting a sputtering efficiency which is a factor of 10 lower than the canonical one. This result confirms the claim of hydrodynamic cosmological simulations (Gjergo et al. 2018; Vogelsberger et al. 2019). The total cosmic dust budget also grows with time, and we argue that more observations of extra-galactic dust, especially at $z \sim 0$, are needed to constrain this quantity better.

Our main conclusion is that the observed decrease of the galactic dust budget at $z \lesssim 1$ may be reproduced assuming canonical prescriptions for dust production and evolution. This drop is enhanced by our treatment of disc instabilities and SMBH growth, which promotes

the suppression of highly SF, dust rich galaxies at $z = 0$, providing a better match of the observed local galactic dust abundance. However, although we presented a reasonable model of SMBH growth during disc instabilities, we also speculate that a comparable result could be obtained with different prescriptions. Indeed, many processes may affect the gas content of these galaxies. For instance, SMBH feedback may cause AGN-driven outflows while in the present model, it only brakes gas cooling.

DATA AVAILABILITY

The data used for this paper will be shared on reasonable request to the corresponding author.

REFERENCES

Almeida J. S., Pérez-Montero E., Morales-Luis A. B., Muñoz-Tuñón C., García-Benito R., Nuza S. E., Kitaura F. S., 2016, ApJ, 819, 110

Andreani P., Miyamoto Y., Kaneko H., Boselli A., Tatematsu K., Sorai K., Vio R., 2020, A&A, 643, L11

Angulo R. E., Hilbert S., 2015, MNRAS, 448, 364

Angulo R. E., White S. D. M., 2010, MNRAS, 405, 143

Aoyama S., Hirashita H., Nagamine K., 2020, MNRAS, 491, 3844

Aoyama S., Hou K.-C., Hirashita H., Nagamine K., Shimizu I., 2018, MNRAS, 478, 4905

Aoyama S., Hou K.-C., Shimizu I., Hirashita H., Todoroki K., Choi J.-H., Nagamine K., 2017, MNRAS, 466, 105

Asano R. S., Takeuchi T. T., Hirashita H., Inoue A. K., 2013, Earth Planets Space, 65, 213

Athanassoula E., 2008, MNRAS, 390, L69

Baldry I. K. et al., 2012, MNRAS, 421, 621

Beeston R. A. et al., 2018, MNRAS, 479, 1077

Bertocco S., Major B., Dowler P., Gaudet S., Molinaro M., Taffoni G., 2019, in Molinaro M., Shortridge K., Pasian F., eds, ASP Conf. Ser. Vol. 521, Astronomical Data Analysis Software and Systems XXVI. Astron. Soc. Pac., San Francisco, p. 61

Bianchi S., Schneider R., 2007, MNRAS, 378, 973

Bournaud F., Dekel A., Teyssier R., Cacciato M., Daddi E., Juneau S., Shankar F., 2011, ApJ, 741, L33

Boylan-Kolchin M., Ma C.-P., Quataert E., 2005, MNRAS, 362, 184

Boylan-Kolchin M., Springel V., White S. D. M., Jenkins A., Lemson G., 2009, MNRAS, 398, 1150

Burke J. R., Silk J., 1974, ApJ, 190, 1

Chabrier G., 2003, PASP, 115, 763

Christodoulou D. M., Shlosman I., Tohline J. E., 1995, ApJ, 443, 551

Covington M., Dekel A., Cox T. J., Jonsson P., Primack J. R., 2008, MNRAS, 384, 94

Croton D. J. et al., 2006, MNRAS, 365, 11
Croton D. J. et al., 2016, ApJS, 222, 22
Dayal P. et al., 2022, MNRAS, 512, 989
De Lucia G., Fontanot F., Wilman D., Monaco P., 2011, MNRAS, 414, 1439
De Vis P. et al., 2019, A&A, 623, A5
Debattista V. P., Mayer L., Carollo C. M., Moore B., Wadsley J., Quinn T., 2006, ApJ, 645, 209
Desert F. X., Boulanger F., Puget J. L., 1990, A&A, 500, 313
Devergne T. et al., 2020, A&A, 644, A56
Dimauro P. et al., 2022, MNRAS, 513, 256
Driver S. P. et al., 2012, MNRAS, 427, 3244
Driver S. P. et al., 2018, MNRAS, 475, 2891
Dudzevičiūtė U. et al., 2020, MNRAS, 500, 942
Dunne L. et al., 2011, MNRAS, 417, 1510
Dwek E., 1998, ApJ, 501, 643
Dwek E., Werner M. W., 1981, ApJ, 248, 138
Efstathiou G., Lake G., Negroponte J., 1982, MNRAS, 199, 1069
Elbaz D. et al., 2007, A&A, 468, 33
Ferrara A., Peroux C., 2021, MNRAS, 503, 4537
Ferrara A., Viti S., Ceccarelli C., 2016, MNRAS, 463, L112
Fisher D. B. et al., 2013, Nature, 505, 186
Fisher D. B., Drory N., 2011, ApJ, 733, L47
Fletcher T. J., Saintonge A., Soares P. S., Pontzen A., 2020, MNRAS, 501, 411
Fu J. et al., 2013, MNRAS, 434, 1531
Fu J., Guo Q., Kauffmann G., Krumholz M. R., 2010, MNRAS, 409, 515
Gail H.-P., Zhukovska S. V., Hoppe P., Trieloff M., 2009, ApJ, 698, 1136
Galliano F., Galametz M., Jones A. P., 2018, ARA&A, 56, 673
Gioannini L., Matteucci F., Vladilo G., Calura F., 2017, MNRAS, 464, 985
Gjergo E., Granato G. L., Murante G., Ragone-Figueroa C., Tornatore L., Borgani S., 2018, MNRAS, 479, 2588
Granato G. L. et al., 2021, MNRAS, 503, 511
Granato G. L., De Zotti G., Silva L., Bressan A., Danese L., 2004, ApJ, 600, 580
Granato G. L., Lacey C. G., Silva L., Bressan A., Baugh C. M., Cole S., Frenk C. S., 2000, ApJ, 542, 710
Graziani L., Schneider R., Ginolfi M., Hunt L. K., Maio U., Glatzle M., Ciardi B., 2020, MNRAS, 494, 1071
Henriques B. M. B., Thomas P. A., Oliver S., Roseboom I., 2009, MNRAS, 396, 535
Henriques B. M. B., White S. D. M., Thomas P. A., Angulo R., Guo Q., Lemson G., Springel V., Overzier R., 2015, MNRAS, 451, 2663
Henriques B. M. B., Yates R. M., Fu J., Guo Q., Kauffmann G., Srisawat C., Thomas P. A., White S. D. M., 2020, MNRAS, 491, 5795
Hirashita H., 2013, in Proc. Sci., The Life Cycle of Dust in the Universe: Observations, Theory, and Laboratory Experiments (LCDU2013). SISSA, Trieste, p. 27
Hirashita H., 2015, MNRAS, 447, 2937
Hirashita H., Kuo T.-M., 2011, MNRAS, 416, 1340
Hirashita H., Yan H., 2009, MNRAS, 394, 1061
Hou K.-C., Aoyama S., Hirashita H., Nagamine K., Shimizu I., 2019, MNRAS, 485, 1727
Huško F., Lacey C. G., Baugh C. M., 2022, MNRAS, 518, 5323
Irodotou D., Thomas P. A., Henriques B. M., Sargent M. T., Hislop J. M., 2019, MNRAS, 489, 3609
Isobe Y. et al., 2021, ApJ, 918, 54
Izquierdo-Villalba D., Bonoli S., Dotti M., Sesana A., Rosas-Guevara Y., Spinoso D., 2020, MNRAS, 495, 4681
Jones M. G., Haynes M. P., Giovanelli R., Moorman C., 2018, MNRAS, 477, 2
Katsianis A. et al., 2020, MNRAS, 500, 2036
Kauffmann G., Haehnelt M., 2000, MNRAS, 311, 576
Koutsouridou I., Cattaneo A., 2022, MNRAS, 516, 4194
Krumholz M. R., McKee C. F., Tumlinson J., 2009, ApJ, 693, 216
Lacey C. G. et al., 2016, MNRAS, 462, 3854
Lagos C., Tobar R. J., Robotham A. S. G., Obreschkow D., Mitchell P. D., Power C., Elahi P. J., 2018, MNRAS, 481, 3573
Lange R. et al., 2015, MNRAS, 447, 2603
Li Q., Narayanan D., Davé R., 2019, MNRAS, 490, 1425

McConnell N. J., Ma C.-P., 2013, ApJ, 764, 184
McKee C. F., Krumholz M. R., 2009, ApJ, 709, 308
McKee C., 1989, in Allamandola L. J., Tielens A. G. G. M.eds, Proc. IAU Symp. Vol. 135, Interstellar Dust. Astron. Soc. Pac., San Francisco, p. 431
McKinnon R., Torrey P., Vogelsberger M., Hayward C. C., Marinacci F., 2017, MNRAS, 468, 1505
Ménard B., Fukugita M., 2012, ApJ, 754, 116
Ménard B., Scranton R., Fukugita M., Richards G., 2010, MNRAS, 405, 1025
Moffett A. J. et al., 2016, MNRAS, 462, 4336
Montier L. A., Giard M., 2004, A&A, 417, 401
Murray N., Quataert E., Thompson T. A., 2005, ApJ, 618, 569
Nozawa T., Kozasa T., Habe A., 2006, ApJ, 648, 435
Parente M., Ragone-Figueroa C., Granato G. L., Borgani S., Murante G., Valentini M., Bressan A., Lapi A., 2022, MNRAS, 515, 2053
Peek J. E. G., Ménard B., Corrales L., 2015, ApJ, 813, 7
Péroux C., Howk J. C., 2020, ARA&A, 58, 363
Planck Collaboration (XLIII), 2016, A&A, 596, A104
Planck Collaboration, 2014, A&A, 571, A16
Popping G., Péroux C., 2022, MNRAS, 513, 1531
Popping G., Somerville R. S., Galametz M., 2017, MNRAS, 471, 3152
Pozzi F., Calura F., Zamorani G., Delvecchio I., Gruppioni C., Santini P., 2020, MNRAS, 491, 5073
Relaño M. et al., 2022, MNRAS, 515, 5306
Relaño M., Lisenfeld U., Hou K. C., De Looze I., Vílchez J. M., Kennicutt R. C., 2020, A&A, 636, A18
Rémy-Ruyer A. et al., 2014, A&A, 563, A31
Roberts M. S., Haynes M. P., 1994, ARA&A, 32, 115
Romeo A. B., Agertz O., Renaud F., 2022, MNRAS, 518, 1002
Said K., Kraan-Korteweg R. C., Staveley-Smith L., 2019, MNRAS, 486, 1796
Santini P. et al., 2014, A&A, 562, A30
Somerville R. S., Primack J. R., Faber S. M., 2001, MNRAS, 320, 504
Springel V., 2005, MNRAS, 364, 1105
Stevens A. R. H., Croton D. J., Mutch S. J., 2016, MNRAS, 461, 859
Taffoni G., Becciani U., Garilli B., Maggio G., Pasian F., Umana G., Smareglia R., Vitello F., 2020, in Pizzo R., Deul E. R., Mol J. D., de Plaa J., Verkouter H., eds, ASP Conf. Ser. Vol. 527, Astronomical Data Analysis Software and Systems XXIX. Astron. Soc. Pac., San Francisco, p. 307
Thacker C. et al., 2013, ApJ, 768, 58
Tielens A. G. G. M., McKee C. F., Seab C. G., Hollenbach D. J., 1994, ApJ, 431, 321
Tonini C., Mutch S. J., Croton D. J., Wyithe J. S. B., 2016, MNRAS, 459, 4109
Triani D. P., Sinha M., Croton D. J., Pacifici C., Dwek E., 2020, MNRAS, 493, 2490
Tsai J. C., Mathews W. G., 1995, ApJ, 448, 84
Vijayan A. P., Clay S. J., Thomas P. A., Yates R. M., Wilkins S. M., Henriques B. M., 2019, MNRAS, 489, 4072
Vlahakis C., Dunne L., Eales S., 2005, MNRAS, 364, 1253
Vogelsberger M., McKinnon R., O'Neil S., Marinacci F., Torrey P., Kannan R., 2019, MNRAS, 487, 4870
Wakelam V. et al., 2017, Mol. Astrophys., 9, 1
Yamasawa D., Habe A., Kozasa T., Nozawa T., Hirashita H., Umeda H., Nomoto K., 2011, ApJ, 735, 44
Yan H., Lazarian A., Draine B. T., 2004, ApJ, 616, 895
Yates R. M., Henriques B. M. B., Fu J., Kauffmann G., Thomas P. A., Guo Q., White S. D. M., Schady P., 2021, MNRAS, 503, 4474
Yates R. M., Henriques B., Thomas P. A., Kauffmann G., Johansson J., White S. D. M., 2013, MNRAS, 435, 3500
Zhang Y.-C., Yang X.-H., 2019, Res. Astron. Astrophys., 19, 006
Zhukovska S., Gail H.-P., Trieloff M., 2008, A&A, 479, 453
Zwaan M. A. et al., 2003, AJ, 125, 2842

APPENDIX A: DUST PROFILES

The importance of adopting a non-constant $n_{gas}(r)$ in equation (12) (according to equation 13) is demonstrated by the S-to-L radial profile of galaxies, as shown in Fig. A1. The S/L profile is too high in the
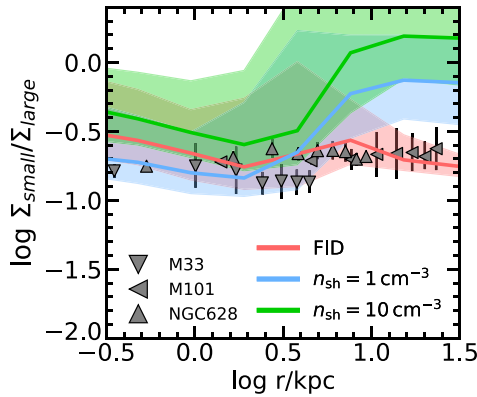
Figure A1. S-to-L median profile (solid lines) and associated 16–84th percentile dispersion (shaded regions) for $z = 0$ disc (B-to-T <0.3) galaxies with $10^9 < M_*/M_\odot < 10^{10.5}$. We show results for our fiducial model, and two models where the number density in equation (12) is assumed to be fixed ($n_{gas} = 1$ and $10\,cm^{-3}$). Results for three local disc galaxies derived by Relaño et al. (2020) are shown as triangles.

Figure B2. Cosmic evolution of galactic dust obtained by models with different $V_{BH,DI}$ (equation (23)). We show the results obtained assuming the same $V_{BH} = 700\,km\,s^{-1}$ in both mergers and instabilities (Vx1), and a $V_{BH,DI}$ larger by a factor 6, 10 and 20 (Vx6, Vx10, Vx20) during disc instabilities. The Vx6 model is the fiducial one adopted in this work (*FID*). We also show the results obtained assuming a constant $f_{BH,unst} = 10^{-4}$ (green line). Results for the model without the new implementation of disc instabilities is shown for comparison (*oldInsta*, grey line). We also show the compilation of observations introduced in Section 3.4.1 (grey shaded region).

outer regions of the galaxies when assuming $n_{gas} = 1$ or $10\,cm^{-3}$. The reason is that these values are excessive for the outer rings. On the contrary, the computation of n_{gas} from $\Sigma_{cold\,gas}$ ensures an almost progressively lower efficiency of shattering with increasing radial distance, as required to match the few available data of local disc galaxies (Relaño et al. 2020).

APPENDIX B: THE IMPACT OF $V_{BH,DI}$

In this section, we show the effect of varying the $V_{BH,DI}$ parameter during disc instabilities introduced in equation (23). Namely, we show the results obtained assuming a $V_{BH,DI}$ during disc instabilities, which is the same as in mergers (Vx1, $700\,km\,s^{-1}$), and larger by a factor of 6, 10, and 20 (Vx6, Vx10, Vx20). We also show the results for a run where we adopt a constant $f_{BH,unst} = 10^{-4}$.

The impact of these choices on the $z = 0$ sSFR distribution in different stellar mass ranges is shown in Fig. B1 (same as Fig. 4). This quantity is particularly convenient for investigating the impact of the SMBH growth on the quenching of galaxies with different masses. For example, when adopting the same V_{BH} in mergers and instabilities (Vx1) we observe a too large quenched galaxies fraction with respect to the star-forming counterparts when compared to SDSS data. Adopting a larger $V_{BH,DI}$ helps to mitigate the SMBH
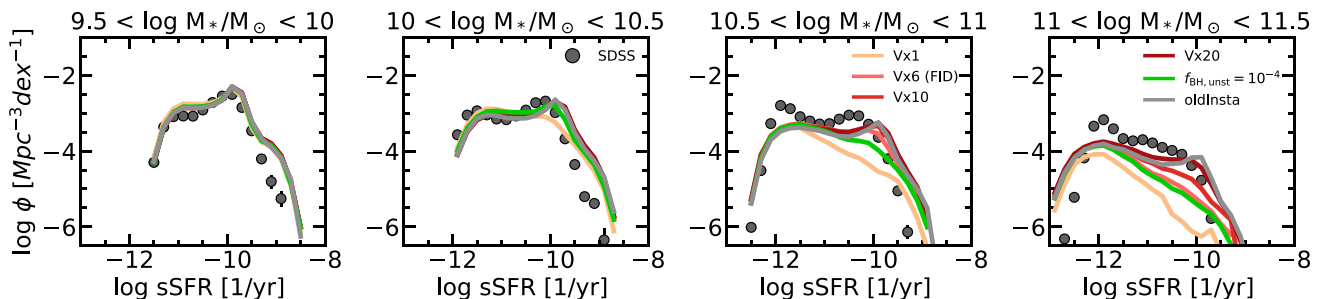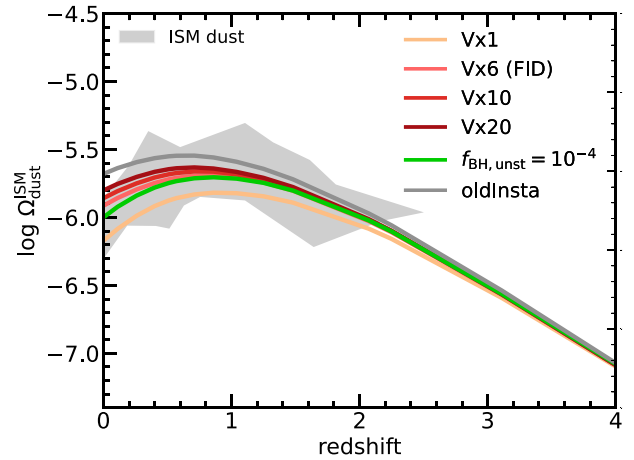
growth and their consequent effect on quenching. In particular, we find that $V_{BH,DI} = 6 \times V_{BH,mergers}$ (Vx6) keeps our model predictions in good agreement with SDSS data for $\log M_*/M_\odot < 11$. Moreover, in the largest stellar mass bin ($11 < \log M_*/M_\odot < 11.5$), the Vx6 model still suppresses the formation of high sSFR galaxies, which are instead obtained in the *oldInsta* model. Similar conclusions may be drawn for the Vx10 model, which unsurprisingly produces a larger number (with respect to the Vx6 model) of high sSFR galaxies in the most massive stellar mass bin. Increasing $V_{BH,DI}$ up to 20 times the value adopted in mergers (Vx20), the sSFR distribution mostly resembles what is obtained in the *oldInsta* model.

As for the $f_{BH,unst} = 10^{-4}$ model, it reproduces quite well the results obtained with our fiducial model broadly, but for a slightly worse agreement with SDSS data in the $10.5 < \log M_*/M_\odot < 11$ bin. This difference has to be ascribed to the V_{vir} dependence, which is adopted in our fiducial model (equation (23)) and ensures SMBH growth to be more effective in more massive systems.
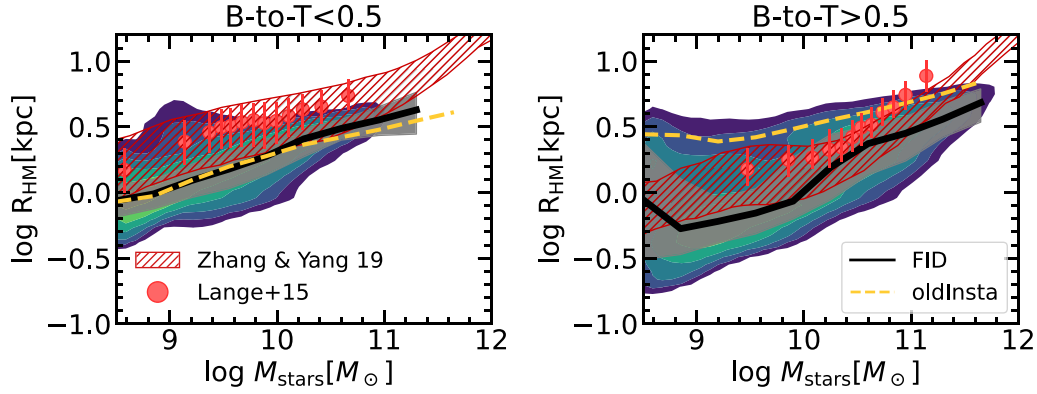

Figure B1. Same as Fig. 4, but for models with different $V_{BH,DI}$ parameters during disc instabilities (equation (23)). Namely, we show the results obtained assuming the same $V_{BH} = 700\,km\,s^{-1}$ in both mergers and instabilities (Vx1), and a $V_{BH,DI}$ larger by a factor 6, 10 and 20 (Vx6, Vx10, Vx20) during disc instabilities. The Vx6 model is the fiducial one adopted in this work (*FID*). We also show the results obtained assuming a constant $f_{BH,unst} = 10^{-4}$ (green line). Results for the model without the new implementation of disc instabilities are shown for comparison (*oldInsta*, grey line).

Figure C1. Stellar half-mass radius as a function of stellar mass for disc-dominated (*left panel*, B-to-T<0.5) and bulge-dominated (*right panel*, B-to-T>0.5). The black line and grey shaded area represent the median and 16–84th percentiles dispersion of our fiducial model results, while log-spaced density contours are shown in background. The median relation obtained by the *oldInsta* model is shown as a gold dashed line. We compare with observations of Lange et al. (2015) (red circles; we use their classification of disc and bulge dominated galaxies according to the Sérsic index) and Zhang & Yang (2019) (hashed red regions, corresponding to the 16–84th percentiles of the observed dispersion).

Finally, we show in Fig. B2 the impact of varying $V_{\rm BH, DI}$ on the cosmic evolution of the galactic $\Omega_{\rm dust}^{\rm ISM}$. As expected from the above discussion, the larger is $V_{\rm BH, DI}$, the lower is the suppression of highly SF galaxies, and thus the higher is the $\Omega_{\rm dust}^{\rm ISM}$ normalization. Similarly, the $f_{\rm BH, unst} = 10^{-4}$ model produces a somewhat stronger $\Omega_{\rm dust}^{\rm ISM}$ drop than the fiducial model, as a result of its slightly stronger SF suppression.

APPENDIX C: GALACTIC SIZES

Here, we briefly discuss the size of the galaxies within our SAM. Although not significantly relevant for the goals of this work, they are affected by the disc instability process, which transfers material from the disc to the bulge, modifying their mass distributions and thus sizes. We take inspiration from Irodotou et al. (2019) for determining the size of bulges formed/grown as a result of both mergers and disc instabilities.

(i) Major mergers

In major mergers, all the pre-existing stars and those formed during the merger, following the collisional starburst formulation by Somerville, Primack & Faber (2001), are added to the bulge of the descendant galaxy. Its half-mass radius $R_{\rm fin, bulge}$ is computed from energy conservation arguments (see also Tonini et al. 2016):

$$\frac{(M_{*,1} + M_{*,2} + M_{*,\rm burst})^2}{R_{\rm fin, bulge}} = \left(\frac{M_1^2}{R_1} + \frac{M_2^2}{R_2} \right) (1 + k_{\rm rad}) + \left(\frac{M_1 M_2}{R_1 + R_2} \right). \quad (C1)$$

In the above formula, M_i are the total baryonic mass of the progenitors, $M_{*,i}$ their total stellar mass, R_i their stellar half-mass radii, and $M_{*,\rm burst}$ the stellar produced in the burst. The term $k_{\rm rad}$ includes energy dissipation by gas due to radiative losses, and it is computed as:

$$k_{\rm rad} = C_{\rm rad} \left(\frac{M_{\rm gas,1} + M_{\rm gas,2}}{M_1 + M_2} \right), \quad (C2)$$

being $M_{\rm gas, i}$ the gas mass of the progenitors, and $C_{\rm rad}$ is a parameter of order $\simeq 1$ (Covington et al. 2008) quantifying the efficiency of radiative losses. Here set to $=1$.

(ii) Minor Mergers

Minor mergers are modelled assuming that the disc of the larger progenitor survives and will host the smaller progenitor's cold gas and the stars formed during the merger-driven starburst. Instead, the larger galaxy's bulge accretes the second progenitor's stars. Its size $R_{\rm fin, bulge}$ is computed according to:

$$\frac{(M_{\rm bulge,1} + M_{*,2})^2}{R_{\rm fin, bulge}} = \left(\frac{M_{\rm bulge,1}^2}{R_{\rm bulge,1}} + \frac{M_{*,2}^2}{R_2} \right) (1 + k_{\rm rad}) + \left(\frac{M_{\rm bulge,1} M_{*,2}}{R_{\rm bulge,1} + R_2} \right). \quad (C3)$$

In the above expression, $M_{\rm bulge, 1}$ and $R_{\rm bulge, 1}$ are the mass and half-mass radius of the bulge of the first progenitor *before* the merger, $M_{*, 2}$ and $R_{*, 2}$ the mass and half-mass radius of the stellar component of the smaller progenitor. The $k_{\rm rad}$ term is computed as in equation (C2).

(iii) Disc instabilities

If the galaxy already possesses a bulge with mass $M_{\rm in}$ and half-mass radius $R_{\rm in}$, the bulge size $R_{\rm fin}$ after a disc instability event leading to a final bulge mass $M_{\rm fin}$ is given by:

$$\frac{M_{\rm fin}^2}{R_{\rm fin}} = \frac{M_{\rm in}^2}{R_{\rm in}} + \frac{M_{\rm unst}^2}{R_{\rm unst}} + \frac{\alpha}{C} \frac{M_{\rm in} M_{\rm unst}}{R_{\rm in} + R_{\rm unst}}, \quad (C4)$$

with $\frac{\alpha}{C} = 1.5$ (C is a structural parameter and α regulates the energy dissipation; Boylan-Kolchin, Ma & Quataert 2005). In the above expression, $M_{\rm unst}$ is the mass of the material transferred from disc to bulge as a result of the instability, and $R_{\rm unst}$ its half-mass radius[19] When a galaxy does not possess a bulge before a disc instability event ($M_{\rm in} = 0$), we simply assume $R_{\rm fin} = R_{\rm unst}$.

In Fig. C1, we show the stellar half-mass radius $R_{\rm HM}$ for disc dominated (B-to-T <0.5) and spheroid dominated (B-to-T >0.5) galaxies. We compare with observations by Lange et al. (2015) and Zhang & Yang (2019). In general, our trends are in broad agreement with the shown data. Nevertheless, our fiducial model predicts a median stellar half-mass radius of disc-dominated galaxies, a factor ~2 lower than observations. We point out that this result is only mildly affected by our implementation of disc instability since a similar behaviour is observed for the *oldInsta* model. As

---

[19]Note that, since the unstable material is already in rings, we can trivially compute the half mass radius of the unstable mass.

for bulge-dominated galaxies, the new computation of bulge sizes introduced in this section improves the performance of our fiducial model in predicting lower stellar half-mass radii, more in line with observations.
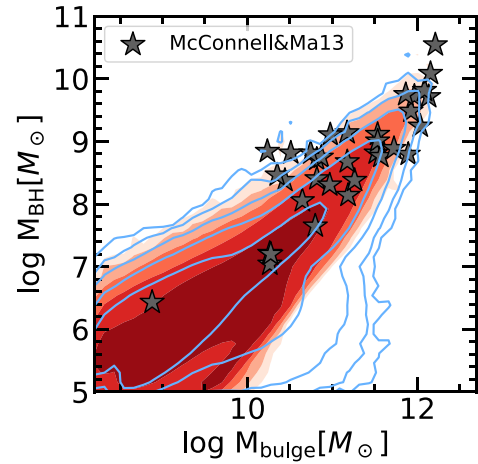

Figure D1. BH-bulge mass relation at $z = 0$ for our fiducial model (log spaced filled red contours of the density of galaxies in this plane) and for the *oldInsta* model (blue contours) compared with observations by McConnell & Ma ([2013](#)).

APPENDIX D: BH-BULGE MASS RELATION

The BH-bulge mass relation at $z = 0$ is shown in Fig. [D1](#) for both the *FID* and *oldInsta* model. The new implementation of BH growth during disc instabilities produces slightly larger BH masses, but still in agreement with most of the observations by McConnell & Ma ([2013](#)).

This paper has been typeset from a TEX/LATEX file prepared by the author.